3D-Printed Hydrogel Composites for Predictive Temporal (4D) Cellular Organizations and Patterned Biogenic Mineralization

*Joselle M. McCracken, Brittany M. Rauzan, Jacob C. E. Kjellman, Mikhail E. Kandel, Yu Hao Liu, Adina Badea, Lou Ann Miller, Simon A. Rogers, Gabriel Popescu, and Ralph G. Nuzzo**

Materials chemistries for hydrogel scaffolds that are capable of programming temporal (4D) attributes of cellular decision-making in supported 3D microcultures are described. The scaffolds are fabricated using direct-ink writing (DIW)—a 3D-printing technique using extrusion to pattern scaffolds at biologically relevant diameters (≤ 100 µm). Herein, DIW is exploited to variously incorporate a rheological nanoclay, Laponite XLG (LAP), into 2-hydroxyethyl methacrylate (HEMA)-based hydrogels—printing the LAP–HEMA (LH) composites as functional modifiers within otherwise unmodified 2D and 3D HEMA microstructures. The nanoclay-modified domains, when tested as thin films, require no activating (e.g., protein) treatments to promote robust growth compliances that direct the spatial attachment of fibroblast (3T3) and preosteoblast (E1) cells, fostering for the latter a capacity to direct long-term osteodifferentiation. Cell-to-gel interfacial morphologies and cellular motility are analyzed with spatial light interference microscopy (SLIM). Through combination of HEMA and LH gels, high-resolution DIW of a nanocomposite ink (UniH) that translates organizationally dynamic attributes seen with 2D gels into dentition-mimetic 3D scaffolds is demonstrated. These analyses confirm that the underlying materials chemistry and geometry of hydrogel nanocomposites are capable of directing cellular attachment and temporal development within 3D microcultures—a useful material system for the 4D patterning of hydrogel scaffolds.

1. Introduction

Technologies that exploit or rely upon principles of selective spatial cellular attachment are numerous and include contact guidance studies, as well as in vivo integration of medical devices and tissue engineering.[1] A deep body of research surrounds the direction of cellular attachment onto specific planar or pseudoplanar substrate geometries, most notably using patterned molecular modifications of substrates, protein treatments, and/or microfabricated device structures to do so.[2] The outcomes of these programmed cellular attachment events include not only the control of internal cellular structures that mediate their structural morphologies but also the biochemical cascades that culminate in cellular behavioral outcomes that can include apoptosis and differentiation.[3]

Advances in the state of the art in the 3D printing of soft, biocompliant materials is engendering new opportunities for the development of materials (and specific chemistries for their modification) that can

Dr. J. M. McCracken, Dr. B. M. Rauzan, J. C. E. Kjellman, Dr. A. Badea, Prof. R. G. Nuzzo
Department of Chemistry
University of Illinois–Urbana Champaign
600 S. Matthews, Avenue, Urbana, IL 61801, USA
E-mail: r-nuzzo@illlinois.edu

M. E. Kandel, Prof. G. Popescu
Department of Electrical and Computer Engineering
4055 Beckman Institute
MC 251, 405 N. Mathews, Urbana, IL 61801, USA

Dr. Y. H. Liu, Dr. L. A. Miller, Prof. R. G. Nuzzo
Frederick Seitz Materials Research Laboratory and
Department of Materials Science and Engineering
University of Illinois at Urbana–Champaign
Urbana, IL 61801, USA

Prof. S. A. Rogers
Department of Chemical and Biomolecular Engineering
University of Illinois–Urbana Champaign
600 S. Matthews Avenue, Urbana, IL 61801, USA

Prof. R. G. Nuzzo
Surface and Corrosion Science
School of Engineering Sciences in Chemistry
Biotechnology and Health
KTH Royal Institute of Technology
Drottning Kristinasväg 51, 100 44 Stockholm, Sweden

The ORCID identification number(s) for the author(s) of this article can be found under https://doi.org/10.1002/adhm.201800788.

DOI: 10.1002/adhm.201800788

be used to precisely program cellular attachment in complex 3D microarchitectural contexts—motifs harboring capacities to sustain and support forms of functional/structural complexity that are not possible with traditional planar substrates.[1e,4] Many of the materials used in 3D printing to date are aimed at achieving either uniform properties of cellular compliance[5] or entirely noncellular applications (e.g., structural composites, electronics, and sensing)[6] such that methods for patterning complex spatial variations of composition to specifically modulate the degree of cellular attachment remain challenges for redress in research. In the case of 3D-printed scaffolds, it is insufficient to universally apply a molecular modification (e.g., a protein or peptide treatment) to achieve spatial control over cellular attachment and compliance since these treatments are difficult to localize and should affect the biocompliance throughout the scaffolds. Furthermore, microcontact printing–based methodologies for patterning cell growth positive ([+]; supporting cellular attachment, spreading, normal motility, and population growth) and negative ([–]; failing to support attachment, spreading, normal motility, and population growth) regions, while powerful, are generally incompatible with 3D scaffolds.[7] In the current work, we focus on engineering a fundamental embedded material biocompliance that can be printed in grayscale forms—that is, with different material compositions acting as points along a spectrum of biocompliance (growth [+] to growth [–])—within 3D architectures at the point of their fabrication. We do so in combination with conjoined materials that provide in hierarchy a functionally distinguishable noncompliance to attachment and growth. The methods and materials described in this report illustrate controlling features and useful approaches to establish scaffolds that manifest discrete states of biocompliance along a spectrum of cellular (+) → (–) growth (and vice versa) within nanocomposite hydrogels that are also rheologically optimized for 3D printing. The variation in biocompliance of these structures affords an exemplary means through which to manipulate, in 4D form, the specifically temporal development of tissue-mimetic organization/functions in 3D cellular cultures.

We utilize direct-ink writing (DIW), an established form of 3D printing using yield-stress fluid inks, to fabricate polymeric scaffold structures in hydrogel materials embedding specific degrees of biocompliance. These DIW inks fall across a range of gray-scale, patternable attributes and modulate properties of growth compliance for cells in contact with them. Inks allowing self-supporting, and thus buildable, filament extrusion at bioactive size regimes with resolutions that are better than 100 μm are described.[4f–o,8] Specifically, we incorporate a rheological modulator, a smectite nanocrystalline disc, Laponite XLG (LAP), into an 2-hydroxyethyl methacrylate (HEMA)-based hydrogel system. This material, LAP–HEMA (LH), is separately compared and joined with a composition, poly(2-hydroxyethyl) methacrylate (pHEMA)–HEMA (pHH), whose rheology is suitably tuned using high molecular weight pHEMA homopolymer as a modifier.[9] Hydrogel materials incorporating LAP and related inorganic additives confer broadly cellular compliant properties to the composites, including robust cellular attachment and (as yet less well understood) impacts on differentiation/development.[10] These properties are ones used in the present work to program complex spatial and temporal attributes of cellular attachment/development in model cultures of NIH/3T3 fibroblast (3T3) and MC3T3-E1 preosteoblast (E1) murine cells, fostering for the latter a capacity to direct long-term osteodifferentiation of the E1 cultures. Cell-to-gel interfacial morphologies are characterized, and LAP-conferred cellular motility is quantitatively analyzed using spatial light interference microscopy (SLIM). Using a combination of pHH and LH gels, we demonstrate a high-performance, high-resolution grayscale patterning of an HEMA-based nanocomposite—UniH—that manifests properties of both gels and allows a dentition-mimetic differentiation of the E1 preosteoblast cultures supported on DIW scaffolds. These analyses confirm that through careful selection and control of the underlying materials chemistry of printed hydrogel nanocomposite filaments, as well as the geometries embedded at the point-of-printing them, it is possible to predict local cellular attachment patterns and subsequent temporal development behaviors within model 3D microcultures. This is an especially useful material system for the 4D printing (4DP) of hydrogel scaffolds for supported cellular assemblies that cannot rely on solution-based or 2D surface modification (e.g., protein) alone to effect spatial control of growth compliance. The current work examines hydrogel materials compositions that innately afford a spectrum of growth compliance affinities that are driven by physiochemical properties rather than post-printing surface treatments.

2. Results and Discussion

2.1. LH Inks and Castable Thin-Film Material Compositions

We have previously described a rheologically exemplary ink for the microscale patterning of HEMA-based hydrogels, pHH-i, whose formulation is summarized in **Table 1** (ID1). The current work extends our earlier studies, utilizing the ink formulation nomenclature deeply studied therein, and here providing a new set of materials chemistries that can afford effective means through which to control and spatially modulate growth compliance in 3D printed scaffolds.[9a,11] The new materials, conjoined with printing-based capacities for grayscale patterning, provide impactful ways to control the temporal evolution of supported 3D microcultures—and offer supporting materials chemistry for biologically compliant 4DP. In biological cultures, the earlier described pHH-i ink behaves as a blank slate material in that cells do not attach to it without a prior activating protein treatment, but for which there is no adverse material attribute that inhibits immediately adjacent cellular attachment, motility, and spreading.[9a] In addition to this printable ink material, we previously described two compositionally distinct, yet closely related, pHH-i-based material compositions (pHH-2 and pHH-4; Table 1, ID2 and ID3) that are amenable to thin-film preparations via spin-casting.[9a] The two film compositions, following treatment with the cellular attachment mediator, poly-L-lysine (PLL; 30k–70k MW), function as oppositional binaries for 3T3 and E1 cellular attachment outcomes, with growth positive conditions found for these cells on treated pHH-2 and growth negative ones on pHH-4. Such programmable states of cellular attachment and development, while useful, do not provide materials compositions suitable for printing-based

Table 1. Printable and castable gel and nanocomposite compositions and growth compliance behaviors for pHH and LH materials.

ID	Name	Print	Cast	Growth PBS	Growth PLL	Chemical components [wt%]										
						HEMA	pHEMA		LAP	PyrPh	DMSO	Irg/DMPA	EGDMA	dH_2O	EtGly	EtOH
							1E6	3E5								
1	pHH-i	+	–	–	+	39.6	9.90	24.75	–	–	–	0.5[b]	1.00	24.25	–	–
2	pHH-2	–	+	–	+	8.83	5.71	2.29	–	–	–	0.22[b]	0.43	5.37	38.57	38.57
3	pHH-4	–	+	–	–	0.69	5.71	2.29	–	–	–	0.02[b]	0.03	2.69	44.28	44.28
4	LH-0	–	–	++	++	3.50	–	–	9.00	–	12.00	0.5[a]	1.00	74.00	–	–
5	LH-i	+	–	++	++	3.50	–	–	9.00	0.20	12.00	0.5[a]	1.00	73.80	–	–
6	LH-1	–	+	++	++	2.66	–	–	6.80	0.28	9.13	0.38[a]	0.76	80.11	–	–
7	UniH[c]	++	–	+	++	9.50	1.65	4.12	7.49	0.21	9.98	0.50[a]	1.00	65.58	–	–

[a]Initiator used specified as either Irgacure or [b]DMPA. (–) negative or not present; (+) positive; (++) superior.; [c]wt% prior to 20% v/w DMSO.

grayscale patterning. The absence of accessible 3D form factors with these compositions ultimately limits their utility for applications in device engineering.

The present work addresses this shortcoming with a new class of printable hydrogel inks that afford superior qualities of biological compliance and printing resolution. The inks here incorporate a rheological viscosifying agent, the nanocrystalline clay LAP, into an otherwise HEMA-based ink composition. The rheology and structural dynamics of LAP-modified hydrogels supporting the present work are discussed in a recent report.[9b] The addition of LAP alone yields useful HEMA-based yield-stress fluid inks (LH-0; Table 1, ID4) with moderate printability, which, once cured, robustly support cell attachment and growth (vide infra). The LH-0 material, though, is prone to jamming during printing and not compatible with the printhead diameters (less than 150 µm) required for meaningful cell localization and attachment patterns. Stable, high-resolution printing is engendered by the addition of low concentrations of sodium pyrophosphate (PyrPh) into the LH ink (LH-i) compositions (Table 1, ID5). The negatively charged PyrPh anion modifies the electrostatic interactions between the LAP platelets, while maintaining a nonjamming microstructure that allows continuous, small diameter printing (<100 µm).[12] Relevant rheological data for the materials used in the present work are given in Section S1 (Supporting Information) along with a comparison of different ink printing behaviors in Video S1 (Supporting Information). To fully complement the pHH hydrogel system, we additionally developed a LAP-based composition, LH-1, that can be used to spin-cast smooth thin films (Table 1, ID6). In the sections that follow, we use this family of gels to prepare a series of grayscale patterns that serve to illustrate functional capabilities for programming (via printing) distinct growth compliance outcomes.

2.2. 3D-Printable Cell Growth Compliance for Juxtaposed Patterns of LH and pHH Materials

The LH and pHH materials afford cell attachment/growth properties of three forms. These are shown for an exploratory pattern series (curvilinear hydrogel filaments printed on a base planar substrate) in **Figure 1**. These forms are 1) universal growth compliance, in which cells grow on both substrate and scaffold (Figure 1a); 2) substrate-only compliance (Figure 1b); and 3) scaffold-only compliance (Figure 1c). For each category of growth, the morphologies are visualized via live/dead assays following seeding with either E1 pre-osteoblast (Figure 1a–c, left two columns) or 3T3 fibroblast (Figure 1a–c, right two columns) cells. Universal growth compliance is achieved for both cell lines by pairing a glass substrate with an LH-i scaffold filament (G/PBS + LHi/PBS; Figure 1a). These conditions produce a growth morphology similar to that achieved using a PLL-treated pHH-2 film to support a treatment-free LH-i filament (pHH2/PLL + LHi/PBS; PLL-based growth outcome controls are given for comparison in Section S2 (Supporting Information)). Substrate-only compliance is seen for both cell lines when LH-1 thin-film substrates are patterned with otherwise untreated pHH-i filaments (LH1/PBS + pHHi/PBS; Figure 1b). Scaffold-only compliance is achieved when LH filaments are printed onto either pHH-2 (pHH2/PBS + LHi/PBS; Figure 1c, row 1) or pHH-4 thin-film (pHH4/PBS + LHi/PBS; Figure 1c, row 2) substrates, data that persuasively demonstrate the differing affinities of pHH and LH materials toward cell attachment and growth. In both cases, we observe that the LH outcompetes other HEMA-based gels in facilitating cellular attachment and growth such that it does not distinguish substantively whether the pHH-type film is the more growth positive material (pHH-2) or the more strongly growth negative variant (pHH-4). For each of the growth profiles shown in Figure 1, normalized fluorescence intensity profiles are plotted that transverse a printed filament, data illustrating the distinct spatial distributions of living cells (green fluorescence) and that of dead cells as convolved with the nonspecific uptake of the dead-cell stain by the thin-film substrates and printed filaments (red fluorescence, gray box showing filament locations in the plots). These measured relative signal intensities are shown in Figure 1d. The data when taken together illustrate that printed patterns provide useful routes for programming specific cellular attachment behaviors (in spatial, and as we show below, temporal domains) in gel-supported cellular microcultures. We next turn to live-cell imaging data to describe the dynamics of these growth outcomes to clarify the mechanisms through which they occur.

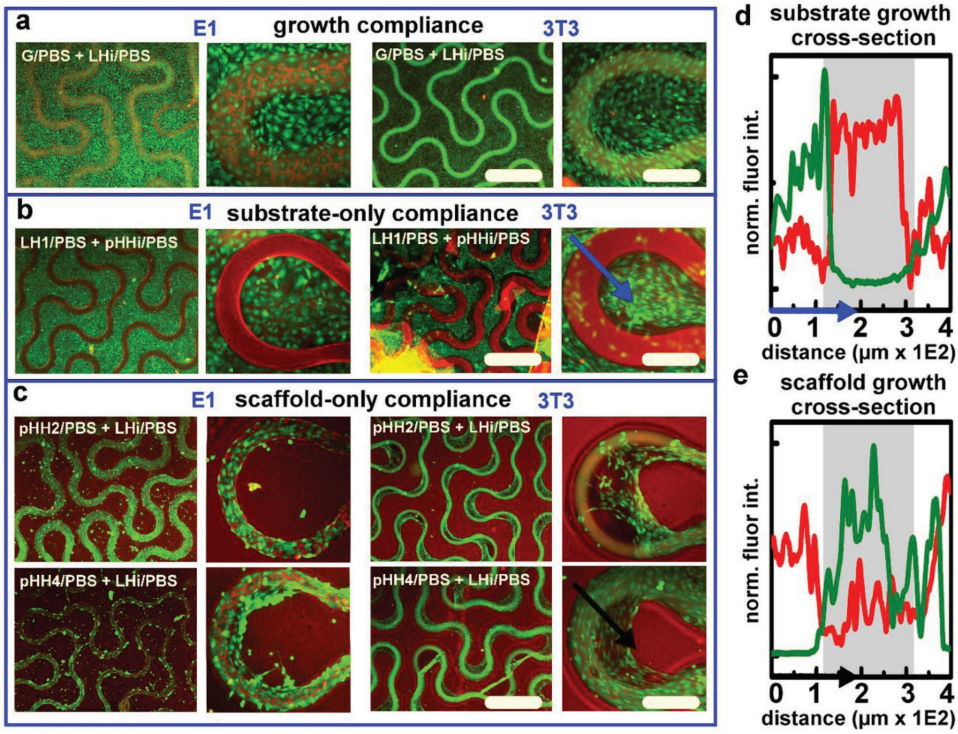

Figure 1. Printed 2D hydrogel patterns rely on material composition to direct cellular growth. Cellular growth compliance tailored for E1 preosteoblast or 3T3 fibroblast cell lines and visualized with a live/dead fluorescence assay at two different magnifications. a) Universal growth on a glass substrate (G) incubated with buffer (PBS), patterned with LAP–HEMA hydrogel ink LH-i, and incubated with PBS. b) Substrate-only growth on an LH-1 film incubated with PBS, then printed with pHH-i, and subsequently incubated in PBS. c) Row 1: Scaffold-only growth compliance on a pHH-2 film incubated in PBS, patterned with LH, and then incubated in PBS. Row 2: A pHH-4 film incubated in PBS, patterned with LH-I, and then incubated in PBS. Cross-sectional normalized fluorescence for red and green channels mapped for d) substrate-only growth and e) scaffold-only growth conditions. Regions marked in gray represent scaffold filaments, with exclusively red signal (top, blue arrow) or exclusively green signal (bottom, black arrow), corresponding to whether scaffold (red) and cell (green) signals are present. Scale bars: 600 μm (low mag) and 150 μm (high mag).

2.3. SLIM of LAP-Driven Cell Attachment Dynamics

The cellular dynamics underlying the growth-compliance trends seen for the LH and pHH materials in both their castable and printable forms are quantified via live-cell imaging using SLIM. This powerful method combines phase contrast microscopy with holography to measure nanoscale structures and dynamics in live cells via interferometry. These capabilities are used in the current work to provide quantitative measurements of E1 and 3T3 cell populations supported on exemplary dichotomous composition LH-i and pHH-i hydrogel scaffolds,[10a] data illustrating features of the inter- and subcellular dynamics underpinning attachment, spreading, and motility over the first 48 h in culture.[13]

Overall, we observe two general cell attachment and migration mechanisms that lead to substrate-only or scaffold-only growth, respectively. **Figure 2**a (left) represents one of these schematically—a substrate-only material environment in which an LH-1 film substrate (light yellow) is overlain with thick, printed microscale pHH-i filaments (pink). In this environment, both E1 and 3T3 cells that initially attach to the filament remain spherical and are poorly adherent (Figure 2a-1, second from left); such cells migrate to the interface between the filament and the substrate at which point they begin to elongate (Figure 2a-2, second from left). The initial localization of cells at the proximal interface of the LH-1 and pHH-i domains is eventually overtaken by migration onto the substrate, where they spread and elongate further (Figure 2a-3, second from left), albeit with displacements that still strongly track along the geometric cues provided by the pHH-i filament. Finally, as they interact with more cells on the substrate, they freely spread and are robustly motile around the entirety of the LH-1 film surface (Figure 2a-4, middle left). Figure 2a (middle right) schematically depicts the second growth motif—a scaffold-only material environment—in which a pHH-4 film substrate (pink) is overlain with printed LH-i gel filaments (light yellow). As the SLIM data show, both E1 and 3T3 cells that initially contact the substrate remain loosely attached and spherical (Figure 2a-1, right), moving along it until they encounter a filament structure. There they begin to elongate near the boundary region between the substrate and scaffold (Figure 2a-2, right), finally elongating along the curvilinear arc of the scaffold filament (Figure 2a-3, right). Finally, the cells spread and divide while remaining robustly motile along the surfaces of the LAP-containing filament, LH-i (Figure 2a-4, right).

In Figure 2b, SLIM image frames for a substrate-only growth condition are given at $t = 0$ h (left) and $t = 48$ h (right) for 3T3 cell culture. Rounded cell bodies adjacent to the filament are

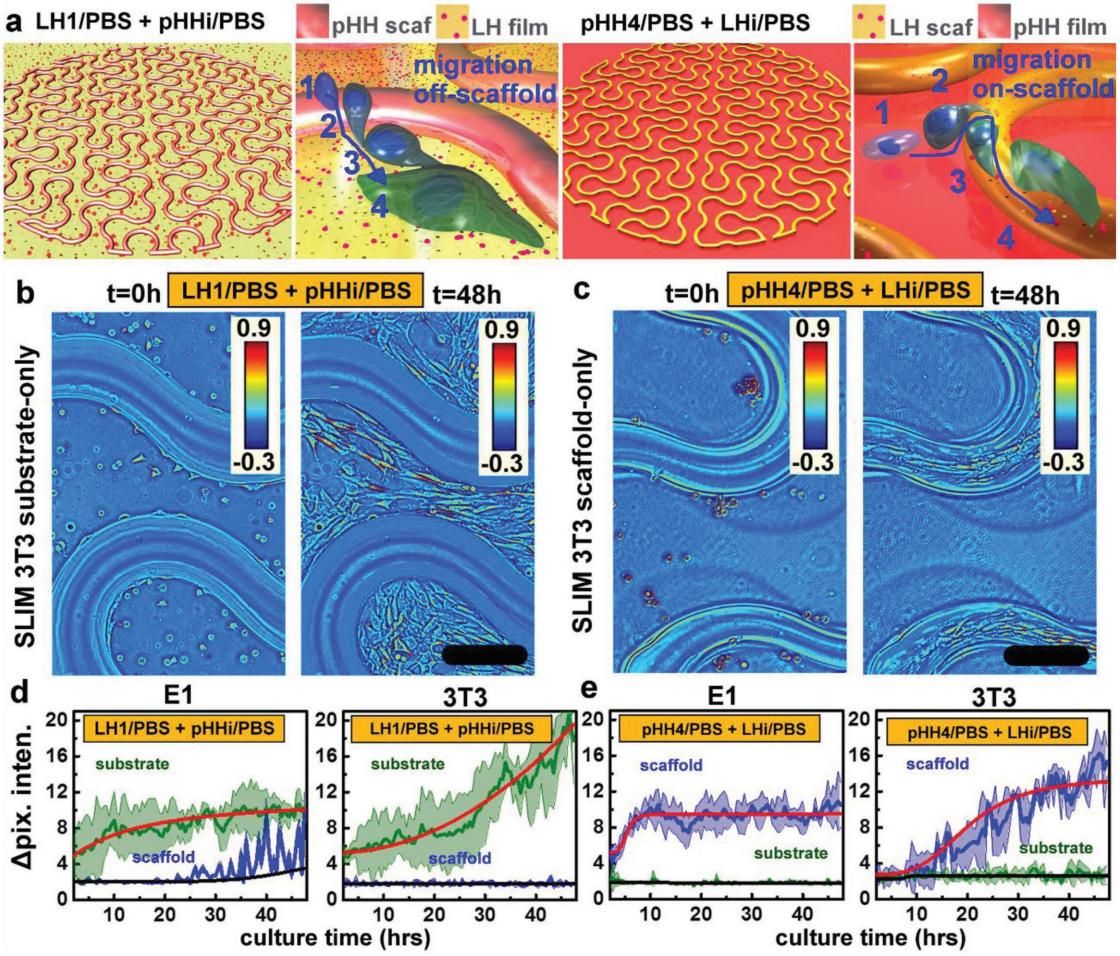

Figure 2. Predictive cellular dynamics tracked with spatial light interference microscopy (SLIM) on printed 2D hydrogel patterns. Protein treatment–free materials with juxtaposed levels of biocompliance direct cellular attachment and growth depending on whether LAP is embedded in the scaffold or in the substrate. a) Schematic of LH-1 films patterned with pHH-i and incubated in PBS (left) to induce cells to attach well only to the substrate. SLIM imaging of E1 preosteoblasts and 3T3 fibroblasts captures their dynamics on these materials (second from left) consisting of 1) loose adhesion on scaffold with spherical morphology, 2) migration to scaffold filament edge with minimal spreading, 3) passage across the interface between scaffold and substrate and elongation, and 4) robust spreading and adhesion on substrate. A schematic of pHH-4 films patterned with LH-i and incubated in PBS (second from right) shows the cellular dynamics as observed with SLIM consisting of 1) rounded cell morphologies loosely adhere and "roll" to scaffold filament edge, 2) some adhesion and elongation of the cell is apparent at the interface, 3) cell passes interface onto filament and elongates, and 4) robust spreading and motility on scaffold. Experimental SLIM images of each case depicted in (a), taken at $t = 0$ and 48 h after seeding cells show: (b) 3T3 cell in-filling substrate selectively and (c) 3T3 cell in-filling scaffold filament selectively. Scale bars 120 µm. Changes in pixel intensity between SLIM video frames measured for both scaffold and substrate contexts are associated with motile and dividing cell motion. SLIM data quantified for E1 and 3T3 cell cultures on the sample given in (d) panel (b), and (e) panel (c). These data show quantitative differences in pixel intensity change that correlates with where cells robustly adhered.

seen appearing to "bud" from the scaffold walls at the first imaged data point, with cells already slightly spreading when they are centrally located on the LH-1 substrate (1 h after applying cells to the scaffolds). By 48 h in culture, near-confluence has been achieved on the substrate, with no growth visible on the filaments themselves. In Figure 2c, representative SLIM image frames for a scaffold-only growth condition are given at $t = 0$ h (left) and $t = 48$ h (right) for 3T3 cell culture. Rounded cell bodies and clusters of floating cells are apparent across the image frame, with several cells seen attaching at the substrate–filament interface. By 48 h in culture, 3T3 cells are seen to be gradually infilling the area of the filament and actively migrating along them. PLL protein treatment controls, additional SLIM images of 3T3 cells, as well as SLIM images of E1 cells are given in Section S3 (Supporting Information), with entire SLIM experiments given as Video S2 (Supporting Information).

To quantify the overall dynamic motion within each culture environment, three representative areas on both scaffold and substrate are selected for both E1 and 3T3 cell lines. The change in their pixel intensity (pixel velocity) between imaging intervals is calculated, and those values averaged at their corresponding time interval in culture. From these data, we first quantitatively verify the stark difference between the pixel velocities that characterize areas in which cells are not seen to attach, spread, and move. We note first here that the changes in pixel velocities (plot

slopes) are not quantitatively distinguishable between cell lines. Even so, these data show robust development of dense/highly motile cell populations from each cell type exclusively in the LAP-presenting region of the scaffold (LH1/PBS + pHHi/PBS in Figure 2d and pHH4/PBS + LHi/PBS in Figure 2e). The E1 cells appear to adhere more strongly to the LH domains than their 3T3 counterparts, in that their overall motility is reduced. We note that the quantitative differences in adherence seen here appears to be specific to this particular pairing of materials, as we have seen cases where (e.g., using protein modifications to promote compliance on pHH substrates) the motilities of E1 and 3T3 cells are more comparable. All the same, these data show that the cell-dependent distinctions in pixel velocity/motility point to the fact that while each cell line responds differently to particular electrostatic and material surface interactions, the directive capability of LH nanocomposites in concert with HEMA gel matrices is a strongly conserved trend seen for both cell types over a broad range of conditions in culture.

Following dynamic characterization of cellular attachment and motility on this scaffold series over the first 48 h post-seeding, periodic imaging is performed to characterize the long-term attachment behaviors of the cells. This is studied under standard culture conditions for 3T3 cells, and in both osteoconductive (OC) and nonconductive (NC) culture environments for E1 cells. Over the first 10 d in culture, the adherent E1 and 3T3 cell cultures largely conserve their highly selective initial attachment localization. In the weeks in culture that follow, the cell populations are generally observed to exceed the area of their preferred anchoring surfaces and gradually lose their selective attachment, with cells continuing to develop until they are confluent throughout their culture environments. Representative images of these cultures that show distribution of the cells and development of mineralization are given in Section S4 (Supporting Information) at 10 d and 4 weeks in culture. These data taken together illustrate how pHH and LH materials may be used to program cellular positions without additional protein treatments or cytotoxic effects and that the two materials fall on opposite ends of the grayscale spectrum of biocompliance. The cell-to-scaffold dynamics over longer term culture intervals as well as the morphology of their biomineralization are also studied and discussed in sections that follow.

2.4. Analysis of Cell-to-Gel Interfaces Formed with LAP-Based HEMA Scaffolds

We used a complimentary set of materials characterization tools to elucidate the basic microstructure formed by an LAP-loaded HEMA hydrogel and the interfaces formed by

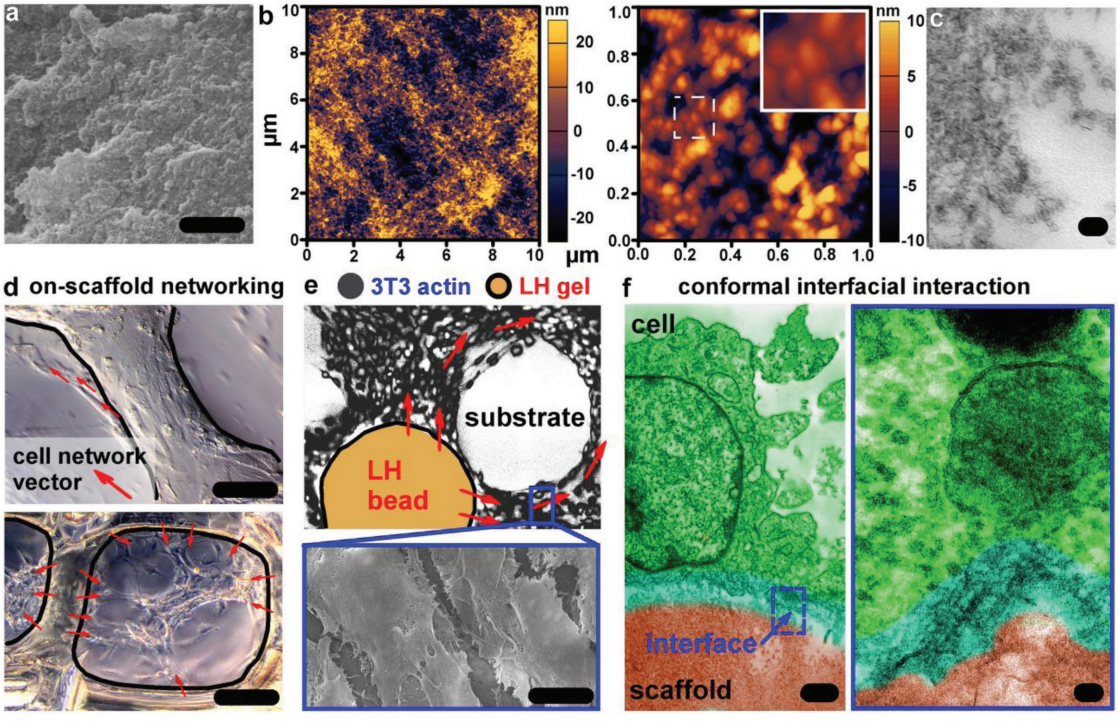

Figure 3. Hydrogel surface nanostructure and cell to gel interfacial morphology. a) Scanning electron microscope (SEM) image of LH-0 gel surface with exemplar qualitative surface roughness in inset (scale bar 1.5 μm). b) Atomic force microscope (AFM) image of LH-0 gel surface over a 10 μm × 10 μm area (left) with gel nanostructure of spheroid aggregates ranging from 20 to 200 nm in diameter (right). Inset of exemplar nanostructure morphology. c) Transmission electron microscope (TEM) section of LH-0 gel edge showing apparent LAP discs that roughen the surface structure of the LH-0 (scale bar 250 nm). d) On-scaffold networking of 3T3 fibroblast cells on grid scaffold filaments (outlined in black) after 24 h (top; scale bar 100 μm) and 96 h (bottom; scale bar 200 μm). Red arrows show cell network vectors as cells interact directly with LH-0 scaffold material. e) LH-0 gel bead surface (orange circle) interaction arrays yield inhomogeneous 3T3 networks with circular open regions where glass substrate is apparent. Overall cell network vectors are given with red arrows. SEM image of 3T3 fibroblasts in these networks shows parallel aligned fibroblast cell bodies at a region proximal to the LH bead surface (scale bar 12 μm). f) TEM shows a 3T3 cell in close conformal attachment to an LH-0 scaffold interface (scale bar 1 μm, left), and a high-magnification image subset (right) shows a 3T3 cell-to-gel interface (scale bar 40 nm).

3T3 cells in contact with it. For these experiments, we used a castable composition, LH-0, that omits the low concentration rheological modifier PyrPh that is required for stable DIW of LH. **Figure 3**a shows an scanning electron microscope (SEM) image representative of a chemically dehydrated gel area section approximately equivalent to the area of one spreading fibroblast. The color-scaled atomic force microscope (AFM) scan shown in Figure 3b (left) is of the air-dried LH-0 gel material taken over a similar area, here showing feature depths spanning a 50 nm range. In Figure 3b (right), a small portion of this gel area is shown that resolves nodule cluster features with a mean grain area of 895 nm^2. The nodule clusters, shown also over a 100 nm area (inset Figure 3b, right) are of a scale consistent with partially exfoliated stacks or nanoaggregates of LAP nanodiscs, with an root mean square (RMS) roughness value of 7.8 nm (additional statistical analyses of AFM images are given in Section S5 (Supporting Information)). The LAP discs residing at the near-ambient surface of the LH-0 thin films are more directly visualized via transmission electron microscope (TEM) sectioning (Figure 3c), in which disperse clusters of LAP discs are seen to form tendril-like/nanoporous structures along the nanocomposite surface. The inset in Figure 3c shows exemplary 25 nm diameter LAP discs as seen at the LH-0 gel boundary. Additional SEM and TEM images of nanocomposite gels are given in Section S6 (Supporting Information).

Aspects of these surface features likely interact in concert with the electrostatic properties of the LAP to encourage robust cellular attachment. On-scaffold networks of 3T3 fibroblasts aligning along the long axis of an LH-0 gel filament are visualized with light microscopy to establish this point, with the data presented in Figure 3d (top). A complementary 3T3 cellular network developing within the open mesh of a grid scaffold manifests multiple anchoring network extensions onto the peripheral nanocomposite filaments, as is seen in Figure 3d (bottom). Vectors plotted in parallel with the 3T3 network extensions present at cell-to-gel interfaces show how frequently these conformations occur in culture. When bead arrays of LH-0 gels are printed onto glass substrates, the effects of the anchored 3T3 network projections become particularly apparent; while semistochastic in nature, we observed with high frequency the occurrence of circular cell-free regions immediately adjacent to the bead interface within an otherwise confluent cellular culture (Figure 3e). These behaviors appear to be causally associated with extremely robust anchoring between the cells and the gel surface, an interaction that in some sense locks the cells into the unusual networking morphologies (shown with red arrows) as appear to define lesser degrees of confluence. An SEM image (Figure 3e, bottom inset) taken of parallel anchored fibroblasts near the perimeter of a cell-free zone shows the tightly parallel alignment present in these regions of the 3T3 cell culture. Additional images of LH-0 bead arrays in cell culture are given in Section S7 (Supporting Information).

To probe the cell-to-gel interface at the nanoscale, a TEM sectioning of 3T3 fibroblasts grown on LH-0 scaffolds is performed. Figure 3f shows a representative colorized TEM section, with the tightly conformal interface (highlighted in turquoise) formed between a 3T3 cell (green) and the LH-0 scaffold (orange) clearly in evidence. Epithelial, myoepithelial and endothelial are the cell types that are known to orient along basement membranes and to secrete the appropriate collagen types to make basement membranes, such as type IV collagen fibrils that anchor them to the basement membrane.[14] In contrast, it is not biotypical for fibroblasts to orient along basement membranes in organ systems,[15] or for them to manifest similar anchoring behaviors, since in normal organ systems they do not attach to basement membranes but exist in the type I collagen and glycoprotein-rich extracellular matrix and use the glycoprotein, fibronectin, to anchor to their surrounding matrix.[15,16] In the high-magnification TEM image (Figure 3f, right inset) of the interfacial interaction between a 3T3 fibroblast and the LH-0 nanocomposite, the nature of their interaction is seen to be extremely conformal, with some evidence of organized cellular structure at that interface. Taken together, these findings point to a cellular attachment and interaction with LAP-rich hydrogels that diverges somewhat from those that occur in normal organ systems, but yet remain capable of exerting substantial control over cellular attachment and growth behaviors.

2.5. 4DP Biogenic Apatite Mineralization via Templated Preosteoblast Growth

We carried out a series of experiments to determine the long-term temporal (4D) direction that LH/pHH scaffolds might exert on more active/responsive cultures. We examined here the interactions between LH/pHH juxtaposed gel microstructures with E1 preosteoblast cultures following osteoconductive (OC) stimulation. Two material systems with discrete biocompliance profiles are examined initially using the loop array microscaffold (vide supra) as a basis for comparison: 1) a printed pHH-i microfilament supported on an LH-1 thin-film substrate (**Figure 4**a) and 2) a printed LH-i microfilament supported on a pHH-4 thin-film substrate (Figure 4b). Cultures of the E1 cells are carried out on scaffolds of each type as exposed to either nonconductive (NC; NC column 1, imaged with light microscopy) or OC media (OC column 2, imaged with light microscopy). For growth on scaffolds of both types, we observed a rather surprising result in the presence of OC stimulation—robust crystal deposition occurring over 7 weeks in culture that is localized almost exclusively on the printed filaments (a pattern that develops irrespective of whether the cells initially attached there or not). Qualitatively, a modest degree of mineralization becomes evident on the relevant scaffolds by 10 d in culture, with mineralization increasing with longer culture intervals. The presence of calcium within these crystals is confirmed using the calcium stain alizarin red (AR), the results for which are shown for a large scaffold section in column 3, with higher magnification imaging of a scaffold filament section in column 4.[17] It is also notable that the morphologies of crystal deposits appear quite distinctive for each scaffold type; though nodular motifs are seen in each case, they are finer for mineralization occurring on a pHH-i filament. (Section S8 (Supporting Information)). The latter habits are, in fact, quite stable and the pHH-i filaments retain their shape and form very durably during extended OC cell cultures. The temporal evolution seen during the mineralization of the LH-i filaments

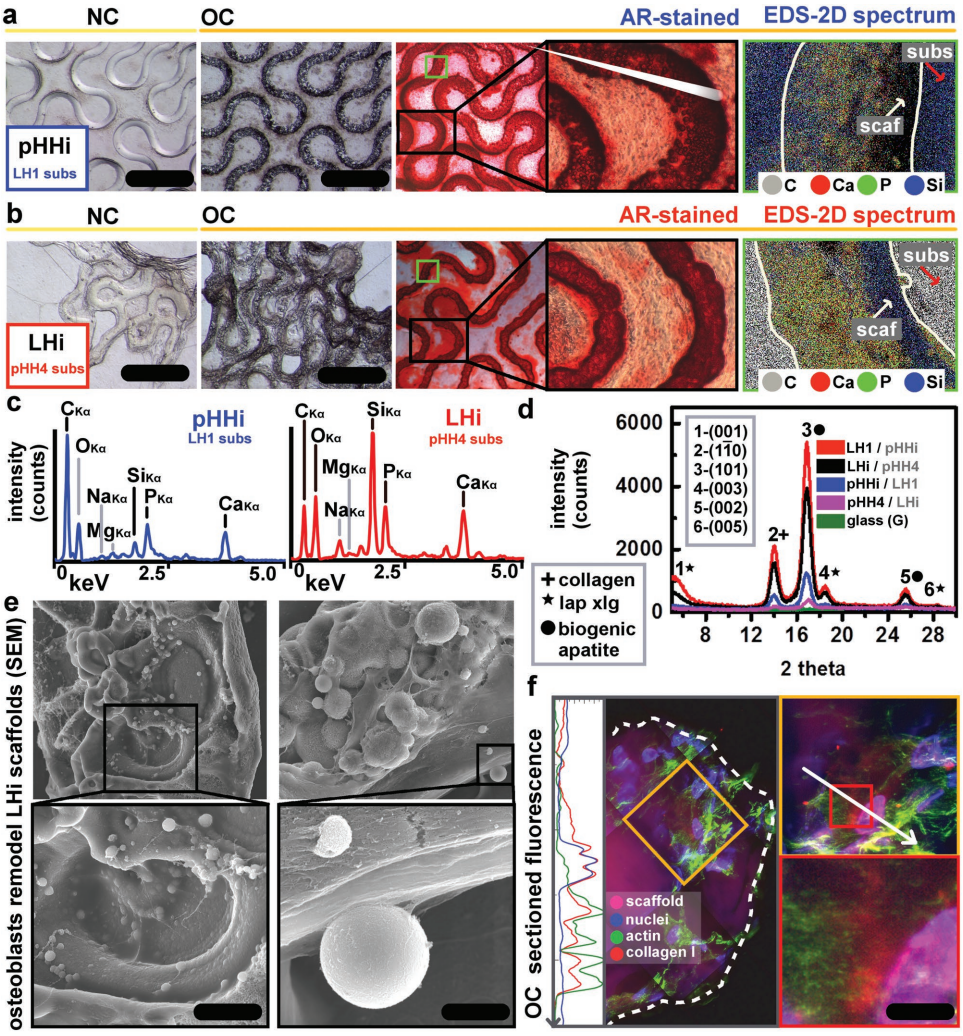

Figure 4. Directed biogenic apatite growth via patterned material composites in 2D differentiated cultures. a) Left: LH-1 patterned with pHH-i after E1 culture in nonconductive (NC) media shows stable gels with no crystal growth. The same scaffold type in conductive media shows selective apatite development after E1 culture (second from left). Scaffolds stained for calcium with alizarin red confirm localization of apatite, given at low and high magnifications (middle and second from right). Energy dispersive spectroscopy (EDS) 2D spectra show Ca and P signals localized on the scaffold filament only. Scale bars 600 µm. b) pHH-4 patterned with LH-i after E1 culture in NC media shows remodeled gel patterns with no crystal growth. The same scaffold type in conductive media shows selective apatite development after E1 culture in conductive media (second from left). Scaffolds stained for Ca with alizarin red confirm localization of apatite at low and high magnifications (middle and second from right). EDS 2D spectra show Ca and P signals localized on scaffold filament. Si in both (a,b) EDS spectra point to the location of the LAP silicates. Scale bars 600 µm. c) EDS spectra with peak assignments for each sample type. d) XRD spectrum lattice assignments and material source (collagen, LAP, or biogenic apatite). Spectra label text is black for the scanned area that was taken in the context of a complementary substrate or scaffold type, specified by gray text. e) SEMs of LH-i scaffolds show cell spreading, material pitting, remodeling, and apatite growth in osteogenic cultures. Scale bar 10 µm. f) CFMs of differentiated cells on sectioned scaffolds (dotted white line) show robust, peripheral attachment, with nonspecific signal from fluorophore adsorption. White arrow corresponds to fluorescence profile trace for channels. Scale bar 2 µm.

is quite different. In this case, the directing LH-i filaments are intensively remodeled by the developing cellular networks and therefore is the more dynamic of the two materials. Complementary SEM/energy dispersive spectroscopy (EDS) 2D spectra of scaffold filaments for each material type (column 5) confirm the suggestions made above about a biogenic mineralization process, here not just the presence, but the on-filament localization of other apatite elements that include phosphorus as well as oxygen, polymeric/organic speciations of carbon, and a strong silicon signal localized wherever LAP nanodiscs loading occurs. These 2D EDS spectra are given in Figure 4c.

To establish the nature of the deposited crystals themselves, we performed a series of X-ray diffraction (XRD) measurements on osteodifferentiated samples that are measured either on- or off-scaffold as well as on an osteodifferentiated glass control. Consistent with the cellular deposition of apatite crystals, the deposited material manifests XRD peaks consistent with biogenic apatite formation along with reflections assignable to an associated/co-deposited collagen matrix and LAP crystals within the LH gel domains (Figure 4d).[18] An SEM imaging analysis is performed specifically on the LH-i filament sample type in order to better characterize its dynamic

early-stage material responses to the developing osteoblast cultures. In Figure 4e, the SEM images on the left examine, at two degrees of magnification, an instance of LH-i filament pitting—structures that are decorated with small apatite crystal deposits. On the right, on-filament osteoblast networks are visible alongside areas that are rich with deposited mineral structures that include medium-to-large spherical apatite-based materials such as the one highlighted in the bottom-right inset. A confocal fluorescence analysis is also performed on a laterally sectioned LH-i microloop array scaffold in which a filament end (outlined with a dotted white line) is coated with differentiated cells, clearly seen from their blue nuclear and green actin stains, around which we also identify some regions of a collagen I protein signal that is not attributable to overlapping fluorescence signals from other cell structures (Figure 4f). Additional supporting cell culture, SEM, AFM, and confocal fluorescence images are given in Sections S9–S12 (Supporting Information).

The outcome of long-term 4D differentiation of E1 preosteoblast cultures provides important insights in the fact that regardless of whether pHH-i or LH-i is used for preparing the 3D-printed scaffold filaments, and regardless of the short-term localization of the preosteoblasts within the culture, the cells consistently deposit biogenic apatite crystals preferentially onto the relief features present within the environment. We also find that from a perspective focused purely on their cellular-response outcomes both LH-i (innately growth compliant and dynamic) and pHH-i (innately growth neutral and stable) contribute uniquely valuable but disparate properties. It is evident from these data that more work needs to be done to deconvolute geometric (filament pattern), material (scaffold and substrate chemistries), spatial (the effect on cellular decision making of pseudo-3D filament walls present within mineralization test cultures), and biochemical gradient effects (filaments acting as vectors to localize and/or change biochemical gradients released by the cells or present within the media) in 2D mineralization cultures. Despite these complexities, we do observe that the large and concentrated biomineral crystallites that are deposited selectively on the scaffold filaments are morphologically distinct from the biomineralization evident on planar, biocompliant OC substrates alone (Section S13 (Supporting Information)). Trends in these data suggest that scaffold filament features affect biocompliance and biomineralization, and that these factors necessitate further study to better predict cellular outcomes in 4D scaffolds made from them.

2.6. pHH and LH Ink Integration for a 4D-Printable HEMA Ink Rheology

The data presented above show very clearly that LH-type materials can strongly, and innately, direct patterns of cell growth. The dynamic reconstruction seen with E1 cells under conditions of OC stimulation suggests that these materials could have useful transient properties that could be exploitable in their own right as controlling materials/cellular attributes are better understood.[19] For this reason, we examined one additional regime of growth, here in the form of E1 cultures under OC stimulation using fully 3D-printed scaffolds as variously formed of LH and pHH materials. The results show strong distinctions in the capacities of these inks to form structurally robust 3D-printed structures. We found that the LH-i material is a quantitatively superior 3D-printable ink, one easily supporting construction of large multifilamentary architectures without flow rate reduction or loss of shape retention. The mesoporous pillar shown in **Figure 5**a (bottom) shows this "buildable" quality and the durable attributes of curvilinear construction (an overlay following the micropattern shown in Figure 2a) it supports. The pHH-i ink is much inferior in this regard and cannot retain its geometry as durably (or at all) with unsupported layers (Figure 5a, top). To test durability in culture at this larger scale, 3D LH-i gel microloop scaffolds (pHH-i cannot be built into 3D structures at a comparable scale) are subjected to long-term E1 cell culture conditions in order to assess the material's stability and biocompatibility over longer intervals in the larger form factor. Exemplary results from these studies, ones performed in either NC or OC media, are shown in Figure 5b. A micro-CT scan of 3D LH-i microloop scaffolds following 16 weeks in culture with E1 cells illustrates the stark differences in biogenic apatite deposition as mediated either by differentiated osteoblasts (Figure 5b, left column OC) and preosteoblasts that have not been differentiated (Figure 5b, right column NC; scaffold humidification chamber given in Section S14 (Supporting Information)). In both cases, we found cell attachment and growth is most pronounced at the outer periphery of the scaffold, even despite the microporosity it embeds (we believe there is minimal cellular penetration into the interior channels due to limits of nutrient perfusion in scaffolds thicker than a few hundred microns).[4j,20] Though robust cellular adhesion around the untreated scaffold periphery is seen in both cases (in accordance with the patterns of cellular attachment seen for LH-1 gel thin films), biogenic mineralization is only pronounced in consequence of OC stimulation (seen as bright white regions in micro-CT scans of OC scaffolds and contrasted by the grayscale background seen for the NC scaffold). As might be expected, the coarser filaments of this scaffold are more durable against the dynamic actions of the culture, although some material degradation is clearly evidenced after more than 14 d in culture. As a result, we explored one additional chemistry that, based on exploratory work, seems to afford a capacity to tune the properties of inks between those of the limiting LH-i and pHH-i compositions.

The ink in this case is a composite comprising components of both of the pHH-i and LH-i gels and affording a complementary rheology. The composition of this universal HEMA ink (UniH, Table 1, ID7) differs most markedly from that of an LH-i ink in that a significant fraction of high molecular weight pHEMA is added to the baseline formulation where it serves as a highly extensible viscosifier and source of crosslinking via entanglement on cure. Extensibility, a rheological property of yield-stress fluids recently described in the literature, has been demonstrated to be a powerful means through which to improve printing performance of inks.[21] This material is able to print continuously and retain its shape robustly across a wide variety of microscale-diameters. These values ranged from 330 μm down to

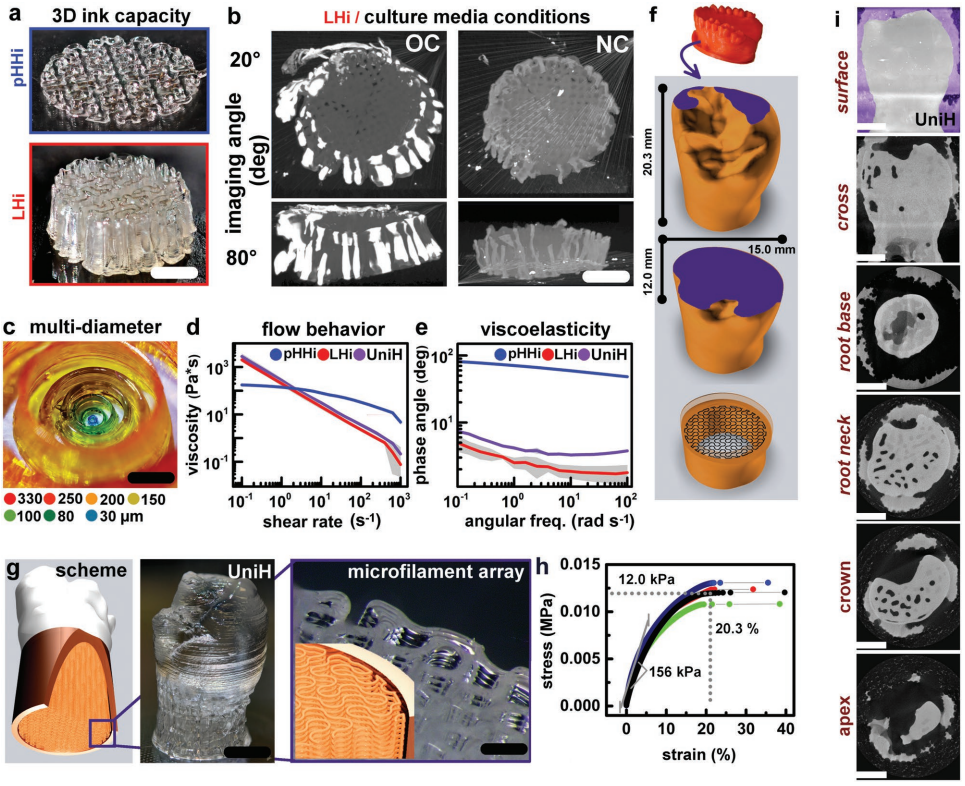

Figure 5. Temporally dynamic 3D-printed scaffold from hybridized LH and pHH hydrogel inks. a) pHH-i is compatible with small diameter printing, but viscoelasticity leads to structural "slumping" that limits the number of 3D layers possible. LH-i is prone to occasional jamming but has higher elasticity and good shape retention of filaments, yielding 3D structure retention. Scale bar 3 mm. b) 3D LH-i scaffolds seeded with preosteoblasts and exposed to either osteoconductive or non-osteoconductive media. Micro-CT imaging at 20° and 80° shows robust biogenic apatite crystal deposition along scaffold walls, with modest penetration into scaffold microstructure. Scale bar 3 mm. c) pHH-i and LH-i combined to prepare UniH ink that resolves printing limitations of each material. UniH ink is compatible with a wide range of printhead diameters (specified by different colors) and is amenable to printing large 3D microstructures. Scale bar 1.2 mm. Rheology comparing d) flow behavior and e) viscoelasticity of pHH-i, LH-i, and UniH inks shows that UniH is more rheologically similar to LH-i. f) Plastic prototype of human dentation used as digital source of single human tooth crown geometry that is modified and integrated with 2D microstructure pattern within root core of scaffold, with overall geometry and exemplar cross-sections of tooth scaffold at intermediate printing layers shown. g) 3D-printed tooth structure schematic (left), with experimental (precure) tooth using UniH ink (middle; scale bar 4 mm). High-magnification image and schematic inset of microfilament array of LAP-based gel printed in the root core microstructure (right). Scale bar 600 µm. h) DMA analysis on UniH gel shows a modulus of 156 kPa with yield at 20% strain. i) Micro-CT of the UniH tooth scaffold after 12 weeks in culture-mimetic fluid at different lateral slices proximal to the 1) root base, 2) root neck, 3) crown, or 4) apex of the tooth scaffold. All images are taken on hydrated samples in a humidification chamber that resulted in some microstructure occlusion due to hydrated cavities, but with structural integrity well maintained by the UniH material over this interval. Scale bar 2.5 mm.

extruded filaments as small as 30 µm, a capacity illustrated in the image of a concentric wall design in which each vertical wall ring is printed with a different printhead diameter and indicating color (Figure 5c). Rheological comparisons of the flow behaviors (Figure 5d) and the viscoelasticities (Figure 5e) of the UniH composition relative to its LH-i and pHH-i progenitors shows it has a striking resemblance to the LH-i composition, but with a slightly higher viscous response across a range of shear rates. The incorporation of an extensible viscosifier results in minor rheological modifications, but actually dramatically improves the 3D printing capacities of the UniH material, allowing significant 3D overlays (200+) microfilaments without observable degradation in flow rate or structure retention.

We illustrate the capacities of this enhanced ink using a human tooth as a model. The CAD design for this demonstration used a pillar-base construction reminiscent of that of the LH-i structure shown in Figure 5a, but adding levels as needed to complete the elements of structure associated with a tooth. The multilevel components required to complete this challenging 3D form factor (one only accessible to the microscale DIW printing capabilities of a high-performance ink such as UniH) are shown in Figure 5f. This architecture has some appeal as an exemplary target for microfilamentary 3D printing in that, in a real tooth, it is a mesoscale biostructure that requires circulation and nerve enervation to fully function but integrates these multifunctional components not nearly at the scale of other organs.[22] Teeth also embed challenging materials gradients, which transition from highly compliant, cell-integrated scaffolding at the root to an impermeable, mechanically loadable crown.[23] Our mimetic scaffold starts with an open microloop matrix in the root region, transitioning therefrom to integrate a high-infill 3D form shaped as a crown (Figure 5f, blue box). The result is an at-scale hybrid hydrogel

nanocomposite scaffold, with the high in-fill crown shown schematically in white and the porous root shown in orange in Figure 5g (left). The actual printed UniH tooth scaffold is shown in Figure 5g (middle), with the structure of the porous microfilament scaffold shown in Figure 5g (right). Dynamic mechanical analyses (DMA; Figure 5h) are performed in quadruplicate on the UniH composite, yielding a modulus for the self-supporting material of 156 kPa, and a yield stress of 12 kPa at 20% strain. While this material is far too compliant for use in tooth crowns, which must sustain extreme, prolonged, and long-term mechanical-loading within the oral cavity, it well illustrates the need for advanced materials chemistries that could in fact fully integrate materials with such disparate physicochemical and mechanical properties. This remains an unsolved challenge of the present work. The UniH scaffold exhibits exceptional stability (with marked improvements over LH-i materials) in aqueous and cell culture environments when tested over a period of more than 12 weeks and imaged in cross-section with micro-CT (Figure 5i).

Finally, we briefly examined general properties of growth compliance on scaffolds comprised of UniH materials. As noted in Table 1 (ID7) and further illustrated in Section S15 (Supporting Information), the UniH materials generally exhibit properties of growth compliance for cells in culture similar to those associated with LH materials. There does appear, however, to exist some processing-centric sensitivity for this attribute, in that some forms of printing yield structures with affinities more closely resembling those of pHH-i scaffolds. We believe a more detailed understanding is needed of the ways in which the hybridized pHEMA and LAP viscosifying agents interact to affect the nanostructure of the UniH ink matrix and their associated biocompliance properties as affect cellular attachment and growth. The accessibility of LAP at the gel to cell contact boundary appears to be the most likely variable at play here. We additionally note that there remains a far more complex requirement for engendering robust forms of growth on a scaffold of the complexity evidenced in Figure 5g, namely the requirement for effective vasculature that can stably support dense 3D in filling. Taken together, the current results illustrate needs for integrating both structure and active forms of function that have the capacity to enable predictive cellular attachment and growth outcomes in fully temporally and spatially/volumetrically dynamic contexts.

3. Conclusion

The capability to direct with high precision cellular attachment, growth, and long-term differentiation within 3D-printed scaffold volumes is one that lags behind the diverse form factors and materials with which such 3D scaffolds can be fabricated with DIW. By incorporating a growth positive inorganic clay nanodisc, LAP, into "blank slate" HEMA hydrogels, we establish a protein-free, materials-based mechanism for conferring directed cellular attachment along 3D-printed gel thin films that vary in their ability to be scaled into truly 3D scaffolds. We characterize the nature of cellular motility as well as cell-to-gel interfacial interactions that drive the programmable attribute of the pHH/LH hydrogel systems and find that in long-term growth experiments we are able to embed the materials properties necessary to induce selective cellular deposition of biogenic apatite crystals. Composites make it possible to modulate growth permissive interactions with cells in culture. The latter point is illustrated with LH and pHH gel compositions that yield a new high-performance material for DIW, termed UniH, which has a 3D fabrication capacity that greatly exceeds its constituent inks' properties. Taken together, these data demonstrate a DIW microscaffold system that is capable—at the point-of-printing—of programming temporally dynamic, 4D cellular attachment outcomes.

4. Experimental Section

Reagent List: Chemical reagents purchased from Aldrich and used as received unless otherwise specified include 2-hydroxyethyl methacrylate monomer (HEMA, 99%, containing 50 ppm monomethyl ether hydroquinone as inhibitor); poly(2-hydroxyethyl) methacrylate (pHEMA-300, average 300 kDa powder); poly(2-hydroxyethyl) methacrylate (pHEMA-1000, average 1000 kDa powder); the radical initiators 2-hydroxy-4′-(2-hydroxyethoxy)-2-methylpropiophenone (Irgacure, IRG, 98%) and 2,2-dimethoxy-2-phenylacetophenone (DMPA, 99%); organic cross-linker ethylene glycol dimethacrylate (EGDMA, 98%, contains 90–110 ppm monomethyl ether hydroquinone as inhibitor, filtered with a prepacked column for removing hydroquinone and monomethyl ether hydroquinone, and stored away from light at 2–5 °C prior to use); dimethyl sulfoxide (DMSO); ethylene glycol (EtGly); trimethoxysilyl propyl(methacrylate); poly-L-lysine hydrobromide (PLL, 30–70 kDa); hydroxyapatite; sodium pyrophosphate; and alizarin red S, certified by the Biological Stain Commission. The ethanol (EtOH) used was of absolute grade (purchased from the University of Illinois stores). Laponite XLG clay was obtained from BYK Additives.

Reagent List for Cellular Subculture: For cellular subcultures, embryonic murine fibroblasts (NIH/3T3 ATCC CRL-1658), Dulbecco's modified Eagle's medium (DMEM), and calf bovine serum (CBS) were purchased from ATCC. For subcultures of murine preosteoblasts (MC3T3-E1 Subclone 14 ATCC CRL-2594), alpha minimum essential media (MEM) without calcium or magnesium, and fetal bovine serum (FBS ATCC 30-2020) were purchased from ATCC. Penicillin-streptomycin (Pen-Strep), Trypsin, and Dulbecco's phosphate buffered saline (DPBS), and alkaline phosphatase detector 1-Step NBT/BCIP were purchased from Life Technologies. Ascorbic acid and beta glycerophosphate disodium salt pentahydrate were purchased from Sigma Aldrich for OC media additives. For cell fixation and fluorescent staining, pH 7, 4% paraformaldehyde-DPBS and 4,6-diamidino-2-phenylindole dihydrochloride (DAPI) were purchased from Polysciences Inc. Normal goat serum (NGS) was purchased from Life Technologies and aliquoted into 200 µL of pure NGS and frozen. Certified 1% Triton X-100 solution, rhodamine–phalloidin (R–P), and Alexa 488 Phalloidin were purchased from Life Technologies. Rabbit polyclonal to Collagen I (anticollagen I antibody reacts with mouse) and goat antirabbit IgG H&L (AlexFluor 555, target species rabbit) were purchased from Abcam Technologies. Fluoro-gel mounting medium was purchased from EMS Acquisition Corp. Image-iT FX signal enhancer was purchased from Thermo Fisher Scientific. Water used in all experiments was purified using a Milli-Q water purification system (Millipore, Bedford, MA) with resistivity higher than 18 MΩ cm. High precision circular 1.5H coverslips from borosilicate glass were purchased from Zeiss Microscopy.

Ink and Film Preparation: The ink and film compositions are detailed in Table 1. Our earlier works in part describe rationales for ink component selections and nomenclature.[9a,11] Briefly, compositional ratios of pHEMA polymer powder relative to HEMA monomer within printable hydrogel inks and films made from them are previously reported to themselves control cellular attachment and motility (−2 → highly growth compliant; −4 → poorly growth compliant). Following

solution-based protein treatments, these materials confer specific degrees of cellular compliance regarding cellular attachment, spreading, and motility. Here, LAP nanoclays are incorporated into HEMA-based inks to extend this work due to their interesting rheological and growth compliant attributes that enable different degrees of biocompliance that function independently from protein or other solution-based surface treatments. The additive NaPyrPh was selected for its capacity to exfoliate the LAP nanodiscs in solution and reduce clumping during printing. It also enables smooth extrusion through smaller printhead diameters that are more relevant to cellular scales.[9b] The relative ratios of each of these components in reported ink compositions was derived from these HEMA-based ink ratios, and modified with LAP, NaPyrPh, and additional solvents through an iterative DIW screening process to develop inks with robust flow properties.

To prepare the inks, the components were hand-mixed upon combination and then fully homogenized using a Thinky Mixer (ARE-310, Thinky) in a closed container at 2000 rpm for 1– 5 min followed by 2200 rpm for 30–60 s. The pHH inks (pHH-i) were prepared and stored away from light and at cool temperatures (stabilities of up to one 1 year were noted) until they were used. For LAP-containing inks, immediately upon LAP addition the vials were strongly hand-shaken to prevent bulk clumping of the LAP, then immediately mixed in the THINKY to fully homogenize them. Only following homogenization were inks stored/equilibrated prior to printing with them. The LH inks were prepared and allowed to sit for 1–3 h prior to printing to allow their rheological stabilization; aging effects were noted in this ink and samples were discarded after 36 h in consequence. The UniH inks were prepared and mixed fully except for addition of LAP and a final addition of DMSO. To complete the preparation of this ink, LAP was added (in the quantity noted in Table 1), and the mixture was allowed to sit for 4–8 h. At that point, a final aliquot of DMSO was added after which printing was initiated within 1–3 h. These inks could be THINKY-mixed after 24 h to rehomogenize the mixture, which enables their continued use for a total of 48 h.

To spin-cast prepolymer solutions of pHH, typically 18–25 mm diameter 1.5H coverslips (Azer Scientific) were thoroughly cleaned with detergent, Milli-Q, acetone, and ethanol in succession. Surfaces were dried with a low fiber cloth (Techwipe) and blown dry with nitrogen. Each pHEMA prepolymer solution of interest was cast at 900 rpm on clean glass substrates and cured under UV illumination for 3 h. LH-1 films were also prepared via spin-casting. To do so, combine 8 g of printable LH-i and to it, add 2.5 mL dH2O + 10 mg NaPyrPh with 2 min THINKY homogenization to prepare a mixture that was immediately spin-castable into films. Spin-cast the films at 3000 rpm for 90 s.

Direct Ink Write Protocols: Prepared inks were loaded into syringes and mounted in an Aerotech AGS-1000 high precision custom gantry with an A3200 integrated automation motion system. The G-Code programming language was used to generate grid scaffold patterns as well as microloop scaffold array designs (vide infra). Code for print paths and the hybrid tooth scaffold design were generated using CAD-Fusion, AutoDesk Inventor, Fusion 360, MeshMixer, and AutoCAD. An Ultimus V High Precision dispenser (Nordson EFD) was used for positive-pressure controlled printing in combination with 3 cc amber light block or clear syringe barrels and 30 µm prepulled glass pipette tip printheads (World Precision Instruments Inc.), or metal barrel luer-lock printheads at 80 (Techcon), 100, or 120 µm diameters (Nordson EFD). An IDS USB 3.0 C-Mount Camera with a color CMOS sensor with a 1.5× Navitar Attachment Lens and a 2.0× Precise Eye Navitar Adaptor Lens (1stVision Inc.) was mounted to the axial stage. Structures were printed on trimethoxysilyl propylmethacrylate-treated high precision coverslips and cured for 1–2 h for pHH compositions, 15–20 min for LH compositions, and for 30–60 min for UniH compositions. A broad-spectrum UV light was used to cure the structures. If a protein treatment was applied, a solution of 5 mg mL^{-1} PLL in PBS was added to scaffolds or films. If the sample in that case was a thin film, the film was allowed to air-dry after at least 30 min of incubation with the protein solution (or a buffer solution control) prior to modification with 3D-printed filaments. When applied to a scaffold/film combination, the scaffold was retreated for at least 30 min with the protein solution, then rinsed 3× with PBS immediately prior to addition of a cell suspension solution.

Cell Culture Protocols: NIH/3T3 (3T3) embryonic murine fibroblasts were maintained in complete media containing DMEM with 10% CBS and 1% penicillin–streptomycin. MC3T3-E1 (E1) preosteoblasts were maintained in complete media containing Alpha MEM, 10% FBS and 1% penicillin–streptomycin. Media compositions selected used were those directly recommended by standard ATCC protocols, with higher nutrient content of FBS specifically suggested for E1 cells and lower nutrient content of CBS recommended for 3T3 cells. For OC media preparation, 1 mL of ascorbic acid and 100 µL of beta-glycerophosphate were added at 50× and 500× their final concentration, respectively. These were 10×10^{-3} M beta-glycerophosphate and 50×10^{-6} M ascorbic acid. At 60–80% confluence, fibroblasts and preosteoblasts were incubated with 3 mL Trypsin for 12 min to achieve complete cell detachment. Resulting solutions were neutralized with 4 mL of complete media and flasks were rinsed with 3 mL DPBS to completely transfer cells prior to centrifugation. Cells of each type were pelleted from solution and resuspended in complete medium prior to scaffold seeding. Subculture was performed to maintain the fibroblast cell line every 2–4 d. Preosteoblasts, upon receipt, were thawed according to the standard ATCC protocol recommendation, then seeded into culture for several days until cell density was higher and has reached approximately 80% confluence. To avoid lowered or altered capacity for E1 cells to undergo osteodifferentation with successive passaging events, at the point of requiring their first passage, the majority of cells were immediately frozen with 20% DMSO in complete media as cryomedia in cryovials. Cell suspensions were first insulated in paper towels and/or plastic bags to slow cooling rates and stored for 15 min in the fridge. Then they were stored for 1–2 h in a freezer. They were then transferred immediately to a −80 °C freezer where they were stored overnight. After 24 h, the cells were transferred to a liquid nitrogen dewar and stored over LN_2 for stable long-term storage. A small portion of cells were subcultured for one more passage then frozen in the same fashion. All cell experiments were performed with cells from one of these batches, with the same batch used for all parallel experiments, to ensure that the degree of osteodifferentiation capacity did not decrease for cells that had been passaged more than 2 times. All cells of each line were maintained at 37 °C at 5.0% medical grade CO_2 throughout the period of cell culture and following seeding onto scaffolds. A Zeiss Axiovert 40 microscope with phase-contrast was used to monitor live cultures. Total cells seeded per well across all experiments ranged from ≈7.5E4 to 1.5E5 cells mL^{-1}. Of note was that certain experimental protocols affected the surface area onto which those cells were able to adhere. For example, certain scaffolds were adhered with a bead of hot glue of variable size. Other specialized cell culture wells for SLIM experiments require reduced necessary diameter values for coverslips or different well-plate diameters.

Live Fluorescence Imaging: All live/dead (L/D) assays were performed at 0.5 mL of 3E5 cells mL^{-1} (1.5E5 cells total per well), while the 2D scaffolds prepared for SLIM measurements as well as long-term mineralization studies were seeded at approximately 0.4 mL of 1.7E5 cells mL^{-1} (7-8E4 cells total per well), or half the density of the L/D experiments, and subsequently allowed to proliferate for 72 h prior to OC transition. The rationale for this difference in seeding density was twofold. First, it was observed from the results of these experiments in parallel that the cells continue to develop into specific attachment/localization patterns at different cell densities. Second, a lowered cell seeding density better facilitates visualization of initial cell motility and patterns of motion at early hours after seeding within SLIM experiments.

Substrate/scaffolds were prepared as described on cleaned coverslips A L/D assay was applied to scaffolds at relevant time points by mixing 5 µL of calcein AM "live" stain and 5 µL of the ethidium homodimer "dead" stain with 10 mL of PBS and incubating all samples chambers in 2–300 µL of this solution during imaging on a Zeiss Axiovert 25 microscope. Cells were protected from light until immediately prior to imaging, and all scaffolds imaged within 3 h of staining.

Calcium and Alkaline Phosphatase Stains: Alizarin red stain (ARS) was prepared by combining 0.7 g of alizarin red powder with 25 mL of Milli-Q water. A pH electrode was used in conjunction with ammonium hydroxide and HCl (as needed) to bring the pH of the solution to a pH of 4.3. The solution was then stored away from light at 4 °C. Scaffolds were stained with ARS that had been allowed to warm to RT by depositing a small volume of the solution onto the sample, allowing it to incubate for 30–60 min, then rinsing copiously but gently with Milli-Q water so as to not disturb fragile cell growth and apatite crystal deposition. Despite ARS binding to LAP nanodiscs in culture to an extent, even when osteodifferentiation had not occurred, this colorimetric stain was selected as an alternative protocol for visualizing mineralization because the LAP itself aggressively adsorbs fluorescent stains in traditional immunostaining protocols, even when blocking agents such as Image-iT FX Signal Enhancer were used, or when extensive nonspecific blocking protocols were used. High filament background signals apparent for cell cultures prepared in this way makes detection of other mineralization-specific secreted proteins within the filaments prone to background fluorescence correction error. For a similar reason, we chose to stain for alkaline phosphatase using another colorimetric stain NBT/BCIP. This NBT/BCIP solution was deposited over the samples and incubated for 30–60 min or until color developed, before being rinsed 3–4× with Milli-Q water. In cases where both stains were used or compared, thin-film scaffolds were severed with a razor blade prior to staining to have parallel stains made across identical sample conditions.

2D Mineralization Experiments: To prepare samples for mineralization experiments, 35 mm Ø well plates were used with the scaffold samples adhered within them using a hot glue bead. The E1 cells were used at concentration of 1.6E5 cells mL^{-1}, and 0.4 mL of E1 cells at this concentration were added to each scaffold/filament sample. To initiate long term OC experiments, 4 mL of OC media was used, with the cultures allowed to develop for 72 h in NC media prior to beginning OC media treatments to increase cell density and facilitate networking in all samples. At 72 h, 2 mL (or 50% by volume) NC media was replaced by OC media, and the following day another 2 mL was removed to be approximately 75% ideal OC concentration in culture. Following this, scaffolds were visually inspected during partial media exchange performed every 2–3 d throughout the culture interval to refresh nutrient levels, but also to retain biochemical signatures that may be present in the culture from the cells. All scaffolds were then maintained in culture for exactly another 7 weeks prior to fixation, staining, and characterization. Progress images were collected throughout these intervals in two consecutively long-term experiment intervals and found qualitatively consistent outcomes for scaffold restructuring and mineral morphologies for each scaffold/substrate combination examined. Images were collected at minimum at 10 d and 4 weeks in culture to minimize stresses on the cultures.

Mineralization becomes apparent to a modest degree on the relevant samples by 10 d in culture, with substantial mineralization apparent by the midpoint of the culture interval, and the qualitative degree of mineralization continues to increase to some degree over the entire culture interval. At the conclusions of culture intervals, to fix and stain the scaffolds, the media in cultures was carefully removed, rinsed 2× with warm (37 °C) PBS buffer, being careful not to physically disturb cultures, then incubated in a third rinse solution of warm PBS buffer. Buffer was next replaced with 1–2 mL of warm 4% PF (aq.) for 0.5 h incubation. Samples were again rinsed 2× with warm PBS. Each sample was carefully broken in half with a glass scribe, and each half was either incubated in either 1 mL of the ARS solution (described in previous section) or 1 mL of the NBT/BCIP solution (described in previous section) for 20 min (or until color develops in NBT/BCIP solution). In this way, staining comparisons were performed on the exact same samples, and not just compositionally comparable samples. After staining, samples were very gently rinsed 3–4× with Milli-Q water. At the termination of the mineralization experiments, each scaffold had been incubated for a total of 52 d (7 weeks + 72 h).

The 7 week mineralization experiments (OC samples) were duplicated with identical cell scaffold compositions, geometries, cell seeding, maintenance, monitoring, rinsing, fixation, and imaging protocols. Prior to these specific experiments, parallel tests of mineralization and colorimetric dyes on osteodifferentiated cultures were performed on molded discs of the materials of interest (≈1 cm in diameter) as well as DIW patterned bead arrays. Comparable trends in dye intensity depending on material and culture environment were observed to those that were later observed in the long-term differentiation experiments. Geometric and interfacial cues at play during these experiments were found to play a role in morphological outcomes that necessitates a uniform controlling of these geometries for more interpretable mineralization outcomes.

SLIM Imaging: For SLIM assays, ≈0.8E5 cells total were seeded into each 35 mm Ø culture well for both E1 and 3T3 experiments to match cellular densities used in long-term mineralization experiments. For one mineralization experiment trial, the SLIM samples themselves were utilized for imaging long term mineralization following the initial SLIM study. The cells were applied to their scaffolds and incubated for 45 min prior to transfer to the SLIM imaging setup. A sealing membrane was applied to prevent cross-contamination during transport. The imaging system consists of a microscope (Zeiss AxioObserver. Z1, 10× NA = 0.3 PN 420341-9911-000) attached to a spatial light interference microscopy module (PhiOptics). In short, this module introduces sequential offsets between transmitted and scattered light by shifting a pattern coupled to the objective's phase ring. The resulting four images were demodulated to yield a phase map with a radian value at each pixel. The module consists of a spatial light modulator (SLM, Meadowlark Optics), sCMOS camera (Zyla 5.5, Andor) along with a polarizer and UV filter. A 6-well plate was loaded with spin-cast pHH-2 or pHH-4 films or glass coverslips that had been incubated in a 0.5 mg mL^{-1} PLL solution or PBS and then patterned with LH-i or pHH-i inks and finally rinsed with PBS or PLL prior to addition of 3T3 or E1 cells that had been grown for 3 d in culture flasks. Each well was imaged with a 10× objective lens in a 3 × 3 grid, with each grid containing 3 focal planes to ensure cell culture capture over longer intervals. The well plate was imaged from 0 to 72 h following seeding from the culture flasks. The media used was the same as that used for the primary cell culture for each cell line. To analyze the SLIM data, each time-lapse frame was tracked using FIJI and MatLab software and the pixel intensity changes from frame to frame were collected, consolidated, and averaged in Excel as a method to quantify the presence or absence of cell structures over a given area in time. From the SLIM data, three 201 × 201 pixel square subsections were collected from both scaffold and substrate regions. Masks were prepared in FIJI that isolated pixel intensity change (pixel velocity) on scaffolds versus substrates within the SLIM images.

SEM Measurements: To prepare samples for SEM, samples were fixed overnight in 4% paraformaldehyde then soaked for another 24 h in DPBS. A 30% EtOH/H_2O was then applied to all samples to begin incremental dehydration. This treatment was followed in succession by rinses using 70% EtOH:H_2O and 100% EtOH solutions. Samples were incubated in each solution concentration for a time not less than 20 min but not extending longer than 1 h. The EtOH solution was then replaced with fresh EtOH solution, followed by overnight sample storage. The samples were next immersed in EtOH/HMDS solution of incrementally high concentration consisting of 2:1 EtOH/HMDS, 1:1 EtOH/HMDS, 1:2 EtOH/HMDS, and 100% HMDS. The samples so treated were allowed to dry overnight. The samples were finally mounted for SEM and sputter-coated for 30 s with Au/Pd prior to imaging with stage rotation and off-center sample loading to maximize angular coverage of the coating. A JEOL 7000F SEM was used to collect the images.

3D Mineralization Experiments: 6 3D LH-i scaffolds of equivalent heights were printed onto pHH film substrate films that were themselves cast onto glass coverslips. The 3D scaffolds were prepared from two different ink batches from discrete (immediately adjacent) mix dates to ensure that the time of printing each scaffold was in a consistent printing age window of the ink material. Because the scaffolds were prepared from different batches, batches from each date of ink preparation were staggered as far as whether they were incorporated into the triplicate series of OC or NC media environments. Triplicate OC and

NC experiments were performed using these 3D scaffolds following a protocol that parallels that used for the 2D scaffold mineralization. Each of the 3D scaffolds were incubated in buffer for 5–12 d after printing but prior to seeding with E1 cells to remove any unreacted components from the nanocomposite scaffold matrix that might inhibit cell attachment or growth. The PBS buffer was removed immediately prior to seeding. During seeding, 0.7 mL of 1.4E5 cells mL^{-1} per well (1E5 cells total per well) That is, concentrated suspended cell aliquots were deposited via micropipette onto the 3D scaffolds, forming a meniscus around the nanocomposite scaffold. The scaffolds were then incubated at 37 °C for an hour while the cells adhered to their scaffold. An additional 4 mL of NC media was then added to begin culture.

The cultures develop for 7 d prior to the additional of OC media to encourage cellular development and integration into the scaffolds. After 7 d, NC media was gradually exchanged in 2 mL aliquots every day with OC media in three of the samples. Prior to incubation in buffer or cell seeding, a hot glue bead was added to attach the coverslip semipermanently to the well plate base. Additionally, a "handle"—or substrate-level filament extending 0.5 cm out from the scaffold bulk—was patterned onto each scaffold that was then also embedded under the hot glue bead. This was to aid in preventing scaffolds from delaminating or experiencing excessive agitation during routine media replacement as their culture time lengthens. The gradual replacement of the media means that it takes several additional days for the OC additive concentrations to be at levels expected to begin OC induction. 3D scaffolds were maintained in culture with their media partially refreshed every 2–3 d for a total of 17 weeks, until the OC 3D scaffolds clearly evidenced mineralization, and the qualitative amount of mineralization was not changing noticeably between observation/media refreshment intervals. Following their time in culture, the 3D scaffolds were optically compared, then apportioned for various characterization protocols, with one entire scaffold from both NC and OC culture condition utilized for L/D assays, ARS stain, or ALP stain. Staining protocols were performed according to the above described procedures. Samples used for L/D assays were also sectioned then used for immunostaining following microsectioning (protocols described in later experimental sections).

Micro-CT Scans: The Xradia Micro-CT (MicroXCT-200) was used to collect micro-CT data for 3D scaffolds after incubation in OC and NC media with preosteoblast cultures. The micro-CT was also used to image complete tooth-mimetic scaffolds prepared from UniH ink and either 1) no enamel-like coating, 2) a commercial epoxy MT-13 adhesive cement (Smooth-On Inc.) coating in the tooth crown, or 3) an in-house composition mixture of artificial enamel made from zinc oxide (ZnO) and 2-ethoxybezoic acid. The latter scaffold types were imaged while hydrated in the micro-CT through use of a custom humidification chamber that utilized water-soaked foam to prevent gel shrinkage during the scan. The system was designed for nondestructive analysis of samples with sub-1 µm pixel resolution possible. The 3D scaffolds of interest were chemically dehydrated using the HMDS dehydration protocol described for SEM analysis above. They were then mounted on a double-sided adhesive to provide stability during the micro-CT measurement. Post processing analyses were performed in Fiji software using the volume viewer plug-in.

TEM Measurements: The cell pellet was fixed in a Karnovsky's fixative in phosphate buffered 2% glutaraldeyde and 2.5% paraformaldehyde. Microwave fixation was used with this primary fixative. The sectioned tissue was next washed in Sorenson's phosphate buffer that contained no further additives. The secondary 2% osmium tetroxide fixative was also prepared via microwave fixation, followed by the addition of 3% potassium ferricyanide for 30 min. Following a water rinse, saturated uranyl acetate was added for enbloc staining. The tissue was dehydrated in a series of increasing concentrations of ethanol. Acetonitrile was used as the transition fluid between ethanol and the epoxy. An infiltration series was made with an epoxy mixture using the epon substitute Lx112. The resulting blocks were polymerized at 90 °C overnight, then trimmed and ultrathin sectioned with a diamond knife. Sections were stained with uranyl acetate and lead citrate, with subsequent microscopic examinations carried out with a Hitachi H600 Transmission Electron Microscope operating at 75 kV.

Microsectioning: In order prepare 3D scaffolds for confocal imaging as well as traditional light imaging, samples were cryogenically frozen and then cut into lateral sections with a microsectioning instrument. Thick scaffolds were still hosting living cell cultures and were transferred to a well plate with warm PBS buffer solution prior to sectioning or they were fixed in paraformaldehyde before being transferred into PBS solutions and some were stained with ARS. To prepare depth profiles across the overall scaffold volume, ultra-thick slices were alternated with a more traditional slice thickness. Here, 500 µm thick sections were cut off and stored in receiving wells. After two of these sections, two 6 µm were prepared and then two 50 µm sections. All samples that had not been previously fixed were then fixed in acetone and mounted on glass slides and stored long-term at −80 °C.

XRD Measurements: XRD measurements were performed using a Pananlytical/Philips X'Pert MRD System with Cu Kα radiation (λ = 0.15418 nm, 45 mA, 40 kV, beam size of 0.5 mm × 0.4 mm). The samples were scanned from 1° to 50° at a scan step rate of 0.025° s^{-1}.

Immunostaining and Confocal Fluorescence Imaging: For immunohistochemical staining, preosteoblast scaffolds were first rinsed in DPBS 3× for 5 min. Image-iT FX Signal Enhancer was deposited onto scaffolds with a dropper to preincubate scaffolds to block nonspecific binding of fluorophores to highly adsorptive LAP within the compositions. The scaffolds were next treated for 3 min with 0.25% Triton X-100 (1 mL of 1% solution to 3 mL of DPBS for 1:4 dilution), then rinsed in DPBS 3× for 5 min. A 5% NGS in DPS solution was then applied to the scaffolds and incubated, followed by another rinse step. An overnight soak was performed of 1:40 primary antibody anticollagen I, with the samples stored at 4 °C during incubation. The rabbit polyclonal antibody to Collagen I (reactive w/mouse) was then added to the samples in a 2% NGS/DPBS solution to incubate, followed by another rinse step. The secondary antibody goat antirabbit IgG (Alexa Fluor 555) 1:200 (to 1:1000) in 2% NGS/DPBS was placed on the sample for 2 h at RT. Next, the conjugated antibody Alexa 488 Phalloidin in 2% NGS/DPBS was applied to the sample for 2 h at RT. DAPI (50 µL of DAPI into 5 mL of DPBS) was then applied to the scaffolds for 1 min. Finally, samples were rinsed with DI water. For all samples, Fluoro-gel (EMS Acquisition Corp.) liquid mounting medium was applied to the scaffolds to prevent photobleaching and to protect the integrity of the scaffold filaments. 25 mm diameter round 1.5H high precision coverslips (Azer Scientific) or 1.5 rectangular coverslips were gently applied over the mounting medium, and samples stored away from light at 4 °C prior to imaging.

All fixed scaffolds were visualized using the Zeiss LSM7 Live CFM. A combination of 10x EC Plan-Neofluar NA 0.3 and 20× objective lenses were used to image large scaffold volumes and required no immersion medium. A 40× NA 1.4 objective lens was used for cell structural analyses, and a 100× Plan Apochromat NA 1.4 objective lens used to image individual morphologies of cellular structures. Both lenses used Zeiss Immersol 518 immersion medium with refractive index n_e = 1.518 at 23 °C. Pinhole diameters for all images ranged from 1 to 2 AU and followed Nyquist sampling rules. Two tracks were used for imaging. Track 1 had an NFT 535 with BP 575-615 + LP 655 in the red channel and BP 495-555 in the green channel. Track 2 had an NFT 565 with a BP 575-615 + LP 655 in the red channel and BP 415-480 in the blue channel. Final images were prepared by combining track 1, channels 1 and 2 with track 2, channel 2; track 2, channel 1 was in duplicate and not used during image processing. The 405, 488, and 550 nm laser excitations were used on fibroblast-seeded scaffolds during imaging. Maximum intensity stacks were generated for each channel and overlaid. Due to the qualitative output that was of interest to this study, channel contrasts were independently adjusted for clarity and fluorescence intensity plot profiles were internally normalized.

Rheological Measurements: A rheometer (DHR-3, TA instruments) with cone-plate geometry (40 mm diameter, 4.005°, 109.5 µm gap height) at 25 °C was used to characterize inks. Three separate samples were taken from a single parent pHH-i preparation, each for separate rheological measurements. For LH-i, three separate samples were prepared with

every component except for LAP. LAP was then added 1 h prior to when the rheological measurement would take place to make the age of the inks constant throughout the triplicate analysis. The oscillation frequency was measured at constant stress (1.0–25.0 Pa) using a logarithmic angular frequency sweep (0.1–100.0 rad s^{-1}). Flow behavior was measured with a logarithmic shear rate sweep (0.1–1000.0 s^{-1}).

AFM Measurements: AFM measurements were performed on an Asylum MFP-3D-SA AFM using BudgetSensors SiNi cantilevers, with image flattening performed using the Asylum Research software. Gwyddion software was used for further postprocessing. For larger scans, a first-order line subtraction was used in addition to a second-order polynomial fit to flatten the image. Smaller scans were primarily flattened using a first-order line subtraction prior to statistical analyses of roughness and 3D rendering of topography in the case of the cell-seeded pHH-i scaffold filament scan.[24] Grain analyses were performed using the grain edge detection algorithm in the Gwyddion software.

Photographic and Light Imaging: Additional images at larger scales were recorded using a Nikon (D90) camera, stereoscope (Olympus, SZX7). The Photoshop photomerge command was used to compile macrostacks from Nikon camera and stereoscope images when needed to obtain large depth of field for macroscale image series.

Supporting Information

Supporting Information is available from the Wiley Online Library or from the author.

Acknowledgements

The authors graciously acknowledge Dr. Debbie Cassout for her expertise, assistance, and advice to prepare microsectioned samples from 3D nanocomposite scaffolds. The authors also thank Dr. Elizabeth A. Driskell for her knowledge and explanation of different cell behaviors in natural organ systems and Dr. David J. Wetzel for his SEM imaging of cell-loaded bead arrays. The authors thank Dr. Kathleen A. Walsh for her AFM scan measurements and image postprocessing. The authors thank Dr. Leilei Yin for his assistance with micro-CT imaging. The authors also thank Prof. Jennifer A. Lewis for her foundational contributions regarding the principles underlying DIW and Dr. A. Sydney Gladman for her instrumental advice for setting up the DIW system. This material was supported by the U.S. Department of Energy, Office of Science, Basic Energy Sciences, under Award No. DE-FG02-07ER46471 through the Frederick Seitz Materials Research Laboratory at the University of Illinois at Urbana–Champaign. J.M.M. developed the principal objectives of the research, conceived of, organized, and implemented the experimental plan, constructed the figures, and wrote the manuscript. J.M.M. performed all cellular experiments, data analysis, and was the lead researcher on all 3D-printing protocols. B.M.R. conceived of and implemented the rheological modifier to enable small diameter printing and performed rheological and XRD measurements. J.C.E.K., with assistance from J.M.M., developed the UniH ink composition. M.E.K. conducted SLIM experiments. Y.H.L. designed the original microloop scaffold array pattern. A.B. contributed parallel procedural knowledge for LAP-related protocols. L.A.M. prepared samples and collected images from TEM. S.A.R. was a principal resource for rheological measurements and analysis. G.P. was a principal resource for SLIM analyses. R.G.N. developed and organized the central guiding principles and foundational approaches for the project overall and the manuscript specifically. All authors contributed to discussion and evaluation of results.

Conflict of Interest

The authors declare no conflict of interest.

Keywords

3D printing, biomineralization, cellular biocompliance, direct ink write 4D printing, hydrogel nanocomposites

Received: July 6, 2018
Revised: October 30, 2018
Published online:

[1] a) C. J. Bettinger, R. Langer, J. T. Borenstein, *Angew. Chem., Int. Ed.* **2009**, *48*, 5406; b) J. Faix, K. Rottner, *Curr. Opin. Cell Biol.* **2006**, *18*, 18; c) X. Dai, W. Zhou, T. Gao, J. Liu, C. M. Lieber, *Nat. Nanotechnol.* **2016**, *11*, 776; d) R. Feiner, L. Engel, S. Fleischer, M. Malki, I. Gal, A. Shapira, Y. Shacham-Diamand, T. Dvir, *Nat. Mater.* **2016**, *15*, 679; e) T. Pong, W. J. Adams, M. A. Bray, A. W. Feinberg, S. P. Sheehy, A. A. Werdich, K. K. Parker, *Exp. Biol. Med.* **2011**, *236*, 366.

[2] a) R. G. Flemming, C. J. Murphy, G. A. Abrams, S. L. Goodman, P. F. Nealey, *Biomaterials* **1999**, *20*, 573; b) M. J. Dalby, M. O. Riehle, D. S. Sutherland, H. Agheli, A. S. Curtis, *Eur. J. Cell Biol.* **2004**, *83*, 159; c) E. T. den Braber, J. E. de Ruijter, L. A. Ginsel, A. F. von Recum, J. A. Jansen, *Biomaterials* **1996**, *17*, 2037; d) J. Mohanraj, L. Puzzi, E. Capria, S. Corvaglia, L. Casalis, L. Mestroni, O. Sbaizero, A. Fraleoni-Morgera, *Mater. Sci. Eng., C* **2016**, *62*, 301; e) S. H. Park, J. W. Hong, J. H. Shin, D.-Y. Yang, *J. Nanomater.* **2011**, *2011*, 9; f) D. T. Chiu, N. L. Jeon, S. Huang, R. S. Kane, C. J. Wargo, I. S. Choi, D. E. Ingber, G. M. Whitesides, *Proc. Nat. Acad. Sci. USA* **2000**, *97*, 2408. g) N. Faucheux, R. Schweiss, K. Lützow, C. Werner, T. Groth, *Biomaterials* **2004**, *25*, 2721. h) G. A. Hudalla, W. L. Murphy. *Soft Matter* **2011**, *7*, 9561.

[3] a) J. Sun, Y. Ding, N. J. Lin, J. Zhou, H. Ro, C. L. Soles, M. T. Cicerone, S. Lin-Gibson, *Biomacromolecules* **2010**, *11*, 3067; b) M. M. Stevens, J. H. George, *Science* **2005**, *310*, 1135; c) E. Cukierman, R. Pankov, D. R. Stevens, K. M. Yamada, *Science* **2001**, *294*, 1708; d) R. Langer, J. P. Vacanti, *Science* **1993**, *260*, 920; e) A. Curtis, C. Wilkinson, *Biomaterials* **1997**, *18*, 1573; f) M. Yoshinari, K. Matsuzaka, T. Inoue, Y. Oda, M. Shimono, *J. Biomed. Mater. Res.* **2003**, *65A*, 359; g) P. Clark, P. Connolly, A. S. Curtis, J. A. Dow, C. D. Wilkinson, *Development* **1990**, *108*, 635; h) A. K. Clark, A. V. Taubenberger, R. A. Taylor, B. Niranjan, Z. Y. Chea, E. Zotenko, S. Sieh, J. S. Pedersen, S. Norden, M. Frydenberg, J. P. Grummet, D. W. Pook, C. Stirzaker, S. J. Clark, M. G. Lawrence, S. J. Ellem, D. W. Hutmacher, G. P. Risbridger, *Biomaterials* **2013**, *34*, 4777; i) L. Chou, J. D. Firth, V. J. Uitto, D. M. Brunette, *J. Cell Sci.* **1995**, *108*, 1563; j) C. S. Chen, M. Mrksich, S. Huang, G. M. Whitesides, D. E. Ingber, *Science* **1997**, *276*, 1425; k) J. H.-C. Wang, B. Li, in *Microscopy: Science, Technology, Applications and Education* (Eds: A. Méndez-Vilas, J. Díaz), Formatex, Badajoz, Spain **2010** pp. 449–458; l) P. Hersen, B. Ladoux, *Nature* **2011**, *470*, 340; m) A. K. Harris, P. Wild, D. Stopak, *Science* **1980**, *208*, 177; n) K. Kuribayashi-Shigetomi, H. Onoe, S. Takeuchi, *PLoS One* **2012**, *7*, e51085; o) V. Maruthamuthu, B. Sabass, U. S. Schwarz, M. L. Gardel, *Proc. Natl. Acad. Sci. USA* **2011**, *108*, 4708; p) Z. Luo, S. Zhang, J. Pan, R. Shi, H. Liu, Y. Lyu, X. Han, Y. Li, Y. Yang, Z. Xu, Y. Sui, E. Luo, Y. Zhang, S. Wei, *Biomaterials* **2018**, *163*, 25; q) Y. Yang, Z. Luo, Y. Zhao, *Biopolymers* **2018**, *109*, e23223; r) Q. Huang, X. Li, T. A. Elkhooly, S. Xu, X. Liu, Q. Feng, H. Wua, Y. Liu, *Colloids Surf., B* **2018**, *169*, 49.

[4] a) G.-H. Wu, S.-H. Hsu, *J. Med. Biol. Eng.* **2015**, *35*, 285; b) R. L. Truby, J. A. Lewis, *Nature* **2016**, *540*, 371; c) C. L. Ventola, *Pharmacol. Ther.* **2014**, *39*, 704; d) J. Klein, M. Stern, G. Franchin, M. Kayser, C. Inamura, S. Dave, J. C. Weaver, P. Houk, P. Colombo,

M. Yang, *3D Print. Addit. Manuf.* **2015**, *2*, 92; e) J. Gardan, *Int. J. Prod. Res.* **2016**, *54*, 3118; f) A. Mahajan, W. J. Hyun, S. B. Walker, G. A. Rojas, J. Choi, J. A. Lewis, L. F. Francis, C. D. Frisbie, *Adv. Electron. Mater.* **2015**, *1*, 1500137; g) J. T. Muth, D. M. Vogt, R. L. Truby, Y. Menguc, D. B. Kolesky, R. J. Wood, J. A. Lewis, *Adv. Mater.* **2014**, *26*, 6307; h) J. J. Adams, S. C. Slimmer, J. A. Lewis, J. T. Bernhard, *Electron. Lett.* **2015**, *51*, 661; i) A. Mahajan, W. J. Hyun, S. B. Walker, J. A. Lewis, L. F. Francis, C. D. Frisbie, *ACS Appl. Mater. Interfaces* **2015**, *7*, 1841; j) D. B. Kolesky, K. A. Homan, M. A. Skylar-Scott, J. A. Lewis, *Proc. Natl. Acad. Sci. USA* **2016**, *113*, 3179; k) J. A. Lewis, B. Y. Ahn, *Nature* **2015**, *518*, 42; l) N. Zhou, C. Liu, J. A. Lewis, D. Ham, *Adv. Mater.* **2017**, *29*, 1605198; m) K. Sun, T. Wei, B. Y. Ahn, J. Seo, S. Dillon, J. A. Lewis, *Adv. Mater.* **2013**, *25*, 4539; n) M. Wehner, R. L. Truby, D. J. Fitzgerald, B. Mosadegh, G. M. Whitesides, J. A. Lewis, R. J. Wood, *Nature* **2016**, *536*, 451; o) C. Cvetkovic, R. Raman, V. Chan, B. J. Williams, M. Tolish, P. Bajaj, M. S. Sakar, H. H. Asada, M. T. A. Saif, R. Bashir, *Proc. Natl. Acad. Sci. USA* **2014**, *111*, 10125; p) T. G. Leong, A. M. Zarafshar, D. H. Gracias, *Small* **2010**, *6*, 792; q) Q. Xu, Y. Lv, C. Dong, T. S. Sreeprased, A. Tian, H. Zhang, Y. Tang, Z. Yu, N. Li, *Nanoscale* **2015**, *7*, 10883; r) S. H. Lee, J. J. Moon, J. L. West, *Biomaterials* **2008**, *29*, 2962; s) S. J. Bryant, J. L. Cuy, K. D. Hauch, B. D. Ratner, *Biomaterials* **2007**, *28*, 2978; t) P. Zorlutuna, N. Annabi, G. Camci-Unal, M. Nikkhah, J. M. Cha, J. W. Nichol, A. Manbachi, H. Bae, S. Chen, A. Khademhosseini, *Adv. Mater.* **2012**, *24*, 1782; u) B. C. Gross, J. L. Erkal, S. Y. Lockwood, C. Chen, D. M. Spence, *Anal. Chem.* **2014**, *86*, 3240; v) T. J. Hinton, Q. Jallerat, R. N. Palchesko, J. H. Park, M. S. Grodzicki, H. J. Shue, M. H. Ramadan, A. R. Hudson, A. W. Feinberg, *Sci. Adv.* **2015**, *1*, e1500758; w) J. C. Nawroth, H. Lee, A. W. Feinberg, C. M. Ripplinger, M. L. McCain, A. Grosberg, J. O. Dabiri, K. K. Parker, *Nat. Biotechnol.* **2012**, *30*, 792; x) A. W. Feinberg, A. Feigel, S. S. Shevkoplyas, S. Sheehy, G. M. Whitesides, K. K. Parker, *Science* **2007**, *317*, 1366.

[5] a) L. Ouyang, C. B. Highley, C. B. Rodell, W. Sun, J. A. Burdick, *ACS Biomater. Sci. Eng.* **2016**, *2*, 1743; b) M. M. Stanton, J. Samitier, S. Sánchez, *Lab Chip* **2015**, *15*, 3111. c) J. Kim, S. McBride, B. Tellis, P. Alvarez-Urena, Y-H. Song, D. D. Dean, V. L. Sylvia, H. Elgendy, J. Ong, J. O. Hollinger, *Biofabrication* **2012**, *4*, 025003; d) Y. Xia, P. Zhou, X. Cheng, Y. Xie, C. Liang, C. Li, S. Xu, *Int. J. Nanomed.* **2013**, *8*, 4197.

[6] a) X. Wang, M. Jiang, Z. Zhou, J. Gou, D. Hui, *Composites, Part B* **2017**, *110*, 442e458; b) H. Chung, S. Das, *Mater. Sci. Eng., A* **2008**, *487*, 251; c) S. J. Leigh, R. J. Bradley, C. P. Purssell, D. R. Billson, D. A. Hutchins, *PLoS One* **2012**, *7*, e49365.

[7] a) J. F. Schumacher, M. L. Carman, T. G. Estes, A. W. Feinberg, L. H. Wilson, M. E. Callow, J. A. Callow, J. A. Finlay, A. B. Brennan, *Biofouling* **2007**, *23*, 55; b) M. L. Carman, T. G. Estes, A. W. Feinberg, J. F. Schumacher, W. Wilkerson, L. H. Wilson, M. E. Callow, J. A. Callow, A. B. Brennan, *Biofouling* **2006**, *22*, 11; c) A. B. Brennan, R. H. Baney, M. L. Carman, T. G. Estes, A. W. Feinberg, L. H. Wilson, J. F. Schumacher, *US Patent 7,143,709*, **2006**; d) L. Hoipkemeier-Wilson, J. F. Schumacher, M. L. Carman, A. L. Gibson, A. W. Feinberg, M. E. Callow, J. A. Finlay, J. A. Callow, A. B. Brennan, *Biofouling* **2004**, *20*, 53; e) A. W. Feinberg, A. L. Gibson, W. R. Wilkerson, C. A. Seegert, L. H. Wilson, L. C. Zhao, R. H. Baney, J. A. Callow, M. E. Callow, A. B. Brennan, in *Synthesis and Properties of Silicones and Silicone-Modified Materials* (Eds: C. Fitzgerald, O. Smith, V. Dyke), ACS Symposium Series, Vol. *838*, American Chemical Society, Washington, DC **2003**, pp. 196–211; f) M. E. Callow, A. R. Jennings, A. Brennan, C. Seegert, A. Gibson, L. Wilson, A. Feinberg, R. Baney, J. Callow, *Biofouling* **2002**, *18*, 229.

[8] J. A. Lewis, *Mater. Matters* **2008**, *3*, 4.

[9] a) J. M. McCracken, A. Badea, M. E. Kandel, A. S. Gladman, D. J. Wetzel, G. Popescu, J. A. Lewis, R. G. Nuzzo, *Adv. Healthcare Mater.* **2016**, *5*, 990; b) B. M. Rauzan, S. E. Lehman, J. M. McCracken, J. Lee, X-M. Lin, S. Narayanan, S. A. Rogers, R. G. Nuzzo, *Adv. Mater. Interfaces* **2018**, *5*, 1701579; c) A. S. Gladman, E. A. Matsumoto, R. G. Nuzzo, L. Mahadevan, J. A. Lewis, *Nat. Mater.* **2016**, *15*, 413; d) E. P. Giannelis, *Appl. Organomet. Chem.* **1998**, *12*, 675; e) Z. Wu, C. Zhou, R. Qi, H. Zhang, *J. Appl. Polym. Sci.* **2002**, *83*, 2403; f) D. R. Katti, P. Ghosh, S. Schmidt, K. S. Katti, *Biomacromolecules* **2005**, *6*, 3276; g) D. Sikdar, D. R. Katti, K. S. Katti, R. Bhowmik, *Polymer* **2006**, *47*, 5196.

[10] a) J. I. Dawson, R. O. Oreffo, *Adv. Mater.* **2013**, *25*, 4069; b) D. Su, L. Jiang, X. Chen, J. Dong, Z. Shao, *ACS Appl. Mater. Interfaces* **2016**, *8*, 9619; c) A. J. Mieszawska, J. G. Llamas, C. A. Vaiana, M. P. Kadakia, R. R. Naik, D. L. Kaplan, *Acta Biomater.* **2011**, *7*, 3036; d) C. Loty, J. M. Sautier, M. T. Tan, M. Oboeuf, E. Jallot, H. Boulekbache, D. Greenspan, N. Forest, *J. Bone Miner. Res.* **2001**, *16*, 231; e) J. R. Xavier, T. Thakur, P. Desai, M. K. Jaiswal, N. Sears, E. Cosgriff-Hernandez, R. Kaunas, A. K. Gaharwar, *ACS Nano* **2015**, *9*, 3109; f) H. Zreiqat, C. R. Howlett, A. Zannettino, P. Evans, G. Schulze-Tanzil, C. Knabe, M. Shakibaei, *J. Biomed. Mater. Res.* **2002**, *62*, 175; g) C. Wang, S. Wang, K. Li, Y. Ju, J. Li, Y. Zhang, J. Li, X. Liu, X. Shi, Q. Zhao, *PLoS One* **2014**, *9*, e99585.

[11] a) A. Badea, J. M. McCracken, E. G. Tilmaand, M. E. Kandel, A. W. Oraham, M. B. Mevis, S. S. Rubakhin, J. V. Sweedler, R. G. Nuzzo, *ACS Appl. Mater. Interfaces* **2017**, *9*, 30318. b) J. N. Hanson Shepherd, S. T. Parker, R. F. Shepherd, M. U. Gillette, J. A. Lewis, R. G. Nuzzo, *Adv. Funct. Mater.* **2011**, *21*, 47.

[12] a) B. Brunier, N. Sheibat-Othman, M. Chniguir, Y. Chevalier, E. Bourgeat-Lami, *Langmuir* **2016**, *32*, 6046; b) A. Pek-Ing, L. Yee-Kwong, *Appl. Clay Sci.* **2015**, *107*, 36.

[13] a) M. Mir, T. Kim, A. Majumder, M. Xiang, R. Wang, S. C. Liu, M. U. Gillette, S. Stice, G. Popescu, *Sci. Rep.* **2015**, *4*, 4434; b) B. Bhaduri, D. Wickland, R. Wang, V. Chan, R. Bashir, G. Popescu, *PLoS One* **2013**, *8*, e56930; c) Z. Wang, L. Millet, M. Mir, H. Ding, S. Unarunotai, J. Rogers, M. U. Gillette, G. Popescu, *Opt. Express* **2011**, *19*, 1016; d) S. Sridharan, M. Mir, G. Popescu, *Biomed. Opt. Express* **2011**, *2*, 2815.

[14] M. Paulsson, *Crit. Rev. Biochem. Mol. Biol.* **1992**, *27*, 93.

[15] C. Frantz, K. M. Stewart, V. M. Weaver, *J. Cell Sci.* **2010**, *123*, 4195.

[16] E. A. Wayner, W. G. Carter, R. S. Piotrowicz, T. J. Kunicki, *J. Cell Biol.* **1988**, *107*, 1881.

[17] a) H. Puchtler, S. N. Meloan, M. S. Terry, *J. Histochem. Cytochem.* **1969**, *17*, 110; b) R. W. Sabnis, *Handbook of Biological Dyes and Stains: Synthesis and Industrial Applications*, John Wiley & Sons, New York **2010**.

[18] a) D. J. Haders, C. C. Kazanecki, D. T. Denhardt, R. E. Riman, *J. Mater. Sci.: Mater. Med.* **2010**, *21*, 1531; b) Y. Cho, J. Hong, H. Ryoo, D. Kim, J. Park, J. Han, *J. Dent. Res.* **2015**, *94*, 491; c) L. N. Niu, K. Jiao, H. Ryou, C. K. Yiu, J. H. Chen, L. Breschi, D. D. Arola, D. H. Pashley, F. R. Tay, *Angew. Chem., Int. Ed.* **2013**, *52*, 5762; d) S. Wang, Y. Wu, R. Guo, Y. Huang, S. Wen, M. Shen, J. Wang, X. Shi, *Langmuir* **2013**, *29*, 5030.

[19] S-W. Hwang, J-K. Song, X. Huang, H. Cheng, S-K. Kang, B. H. Kim, J-H. Kim, S. Yu, Y. Huang, J. A. Rogers, *Adv. Mater.* **2014**, *26*, 3905.

[20] D. B. Kolesky, R. L. Truby, A. S. Gladman, T. A. Busbee, K. A. Homan, J. A. Lewis, *Adv. Mater.* **2014**, *26*, 3124.

[21] a) A. Z. Nelson, R. H. Ewoldt, *Soft Matter* **2017**, *13*, 7578; b) B. M. Rauzan, A. Z. Nelson, S. E. Lehman, R. H. Ewoldt, R. G. Nuzzo, *Adv. Funct. Mater.* **2018**, *28*, 1707032.

[22] a) D. V. Provenza, *Circ. Res.* **1958**, *6*, 213; b) L. Edwall, M. Kindlová, *Acta Odontol. Scand.* **1971**, *29*, 387; c) A. G. Fincham, J. Moradian-Oldak, J. P. Simmer, *J. Struct. Biol.* **1999**, *126*, 270.
[23] a) R. L. Woods, P. M. Kildea, S. A. Gabriel, L. S. Freilich, *Oral Surg., Oral Med., Oral Pathol.* **1984**, *58*, 82; b) S. Tauscher, *Dent. Mater.* **2017**, *33*, 857; c) R. M. Carvalho, J. Mendonca, S. Santiago, R. Silveira, F. Garcia, F. Tay, D. H. Pashley, *J. Den. Res.* **2003**, *82*, 597; d) K. Van Landuyt, J. Snauwaert, M. Peumans, J. De Munck, P. Lambrechts, B. Van Meerbeek, *Den. Mater.* **2008**, *24*, 1412; e) K. Van Landuyt, J. De Munck, J. Snauwaert, E. Coutinho, A. Poitevin, Y. Yoshida, S. Inoue, M. Peumans, K. Suzuki, P. Lambrechts, *J. Den. Res.* **2005**, *84*, 183; f) H.-N. Lim, S.-H. Kim, B. Yu, Y.-K. Lee, *J. Appl. Oral Sci.* **2009**, *17*, 340.
[24] D. Nečas, P. Klapetek, *Open Phys.* **2012**, *10*, 181.